

Double restabilization and design of force-displacement response of the extensible elastica with movable constraints

P. KOUTSOGIANNAKIS, D. BIGONI AND F. DAL CORSO*

DICAM, University of Trento, via Mesiano 77, I-38123 Trento, Italy

Dedicated to Natasha and Sasha Movchan on the occasion of their 60th birthday

Abstract

A highly deformable rod, modelled as the extensible elastica, is connected to a movable clamp at one end and to a pin sliding along a frictionless curved profile at the other. Bifurcation analysis shows that axial compliance provides a stabilizing effect in compression, but unstabilizing in tension. Moreover, with varying the constraint's curvature at the origin and the axial vs bending rod's stiffness, in addition to possible buckling in tension, the structure displays none, two, or even four bifurcation loads, the last two associated only to the first buckling mode in compression. Therefore, the straight configuration may lose and recover stability one or two times, thus evidencing single and double restabilization, a feature never observed before. By means of the closed-form solution for the extensible elastica, the quasi-static behaviour of the structure is analytically described under large rotations and axial strain. The presented solution is exploited, together with an *ad hoc* developed optimization algorithm, to design the shape of the constraint's profile necessary to obtain a desired force-displacement curve, so to realize a force-limiter or a mechanical device capable of delivering a complex force response upon application of a continuous displacement in both positive and negative direction.

Keywords: *Euler buckling, tensile buckling, multistability, frictionless constraint.*

1 Introduction

The design of structures displaying a prescribed force-displacement response is a challenge in the engineering of mechanical metamaterials [25, 36, 42, 44]. An important example of such a device is the force-limiter, used to prevent unbounded growth of a force applied to a sensitive element. In this device, when a certain threshold of force is attained, the (incremental) stiffness vanishes, thus allowing the displacement to grow. This occurs until a certain limit stroke is reached, at which the device finally locks. If the force-limiter is purely elastic, dissipation is prevented, so that the displacement decreases back to zero when the force is released. Force-limiting mechanisms may be used to bound the force transmitted during an impact, as is the case of automotive seat belt systems, where plastic deformation developing in mechanical elements prevents reuse of the device [5, 12, 14]. Another crucial application is for vibration isolation of scientific and measuring equipments [1, 20, 30], (e.g. optical tables [38]), or of gravitational-wave detection laboratories [15], but also of civil structures to be shielded from earthquakes [2, 22, 32].

Furthermore, the designed force-displacement curve can be enhanced to exhibit multistability, as in reconfigurable metamaterials for shock absorption [41], shape programming [35], elastic energy trapping [33], and wave guiding [21]. Several structural schemes have been so far proposed for these purposes,

*Corresponding author

E-mail addresses: p.koutsogiannakis@unitn.it, bigoni@ing.unitn.it, francesco.dalcorso@unitn.it

most incorporating negative stiffness elements, such as magnetic springs for active vibration control [31, 45, 46], oblique mechanical springs [13], extremely deformable [37], or buckling [27, 40] beams.

Within this mechanical framework, an innovative structural system, based on tensile and compressive buckling of an elastic rod, is proposed in the present article. More specifically, an axially and flexurally deformable rod is considered with one clamped end constrained to move along a straight direction and the other along a curved profile with a possible discontinuous curvature. The soft rod remains straight until the axial force is sufficiently small, but it buckles (under either compression or tension) and enters in a strongly nonlinear post-critical behaviour, when the load surpasses a critical limit, thus forcing rod deflection. Therefore, in contrast with an inextensible rod, the soft rod deforms axially before buckling, thus allowing to display an initial linear force-displacement response. The considered structural system is analytically solved in its nonlinear range and an optimization algorithm is developed, allowing the design of a desired force-displacement response. As an example of the obtained results, Fig. 1 reports the response of a force-limiting device designed by us and showing an excellent performance. More in general, the force-displacement response of the proposed structure depends only on the constraint's profile shape and on the (axial vs bending) stiffness ratio, so that negative stiffness, or sinusoidal, or triangular, or many other 'exotic' responses can be designed (examples are presented in Section 5).

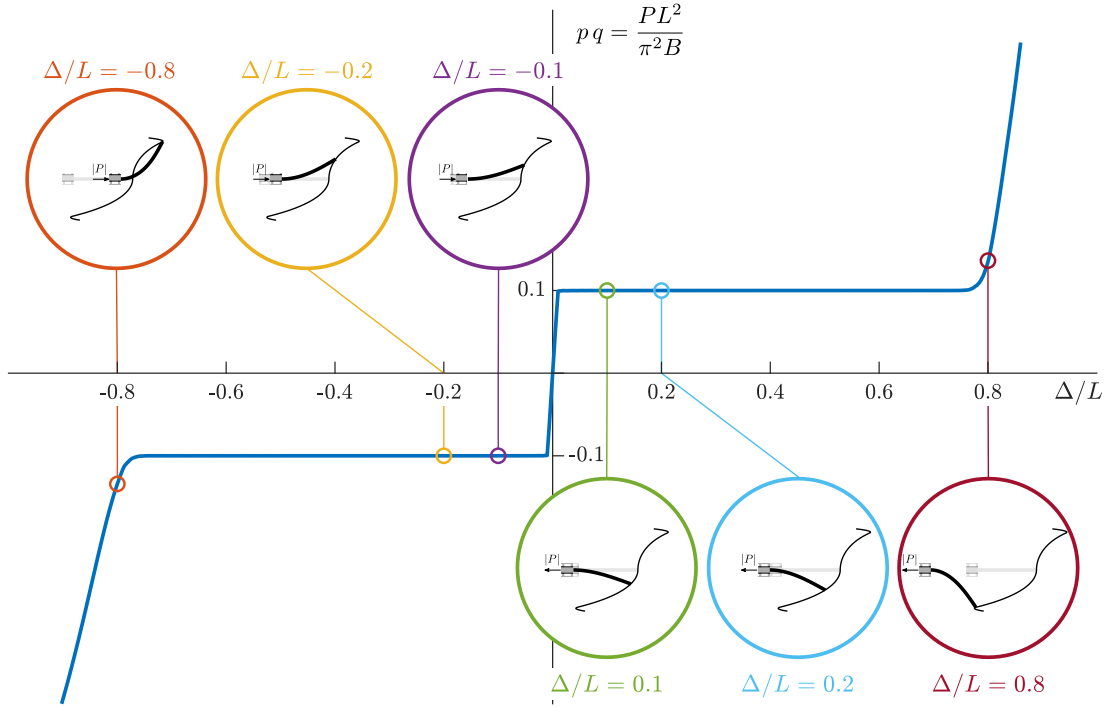


Figure 1: Dimensionless force $PL^2/(\pi^2 B)$ vs. dimensionless displacement Δ/L for an elastic rod (flexurally and axially deformable and subject to a curved constraint), with a stiffness ratio $q = KL^2/(\pi^2 B) = 10$, optimized to realize a force limiter device with $|P_{cr}|L^2/(\pi^2 B) = 0.1$ and locking near the end of the stroke (from $\Delta/L = \pm 0.73$). Deformed configurations of the elastic rod are displayed for $\Delta/L = \pm\{0.1, 0.2, 0.8\}$, along with the optimized shape of the constraint's profile, found to have a discontinuous curvature at the origin ($f''(0^-) = -4.186$ and $f''(0^+) = 1.897$).

The analysis of the proposed structure leads to another important feature, never observed before: the *double restabilization* in compression. Indeed, due to the axial compliance of the rod, it is expected that the straight configuration recovers stability after buckling, similarly to the behaviour of the 'penetrating blade' [7], and therefore displays a restabilization in compression. However, within a specific set of stiffness ratios and profile curvatures at the origin, the proposed structure displays a *double restabilization* of the trivial (straight) configuration, where four exchanges of stability are observed. This unexpected feature is analysed in detail in Section 3, but a concise explanation is anticipated in Section 1.1.

The present theoretical analysis initiates with the derivation of the nonlinear equilibrium equations for the extensible elastica (Sect. 2). Linearization of these equations governs the determination of bifurcation (Sect. 3.1), which is complemented by a stability analysis of the trivial configuration (by means of a dynamic approach, Sect. 3.2). The post-critical response is evaluated analytically by adapting an available closed-form solution [4] to the present boundary conditions (Sect. 4). Finally, an optimization algorithm is developed to find the profile shape displaying a prescribed force-displacement curve (Sect. 5). The solution of this problem is shown to change with varying the (axial vs bending) stiffness ratio, so that many systems can provide the same structural response. Finally, it is shown that a broad range of post-critical behaviours can be achieved (including bilinear, sinusoidal, triangular) and that more axially compliant rods facilitate the optimization.

The results presented in this article can be used in the design of *passive* mechanical devices (i.e. not needing external control), delivering a designed force-displacement response and possibly encompassing multistable behaviour, with applications in the field of force-limiters and soft mechanisms. Movies of the present structure optimized to provide specific force-displacement diagrams are available as electronic supporting material.

1.1 A premise on (single and double) restabilization

Using linearization, a simple explanation is provided below for the destabilization and subsequent restabilization of the straight configuration of an axially and flexurally deformable elastic rod, with a movable clamp at its left end and a pin at the right one, subject to an axial load P that is assumed positive when tensile.

The linearized axial and flexural equilibrium equations are

$$K\varepsilon(S) - P = 0, \quad B\theta''(S) - \left(1 + \frac{P}{K}\right)P\theta(S) = F, \quad (1)$$

where K and B are the axial and bending stiffness respectively, $\varepsilon(S)$ the local axial strain, $\theta(S)$ the rotation of the rod's tangent with respect to the undeformed straight configuration, F is the (unknown) reaction at the pin (orthogonal to P), and the prime denotes the derivative with respect to the undeformed curvilinear rod's coordinate S .¹

The boundary conditions $\theta(0) = 0$, $\theta'(L) = 0$, and $\int_0^L \theta(S) dS = 0$ lead to the following expression for the bifurcation loads

$$\pi \sqrt{-(1+p)pq} \cot\left(\pi \sqrt{-(1+p)pq}\right) = 1, \quad (2)$$

where p is the non-dimensional load and q is the (axial vs bending) stiffness ratio, defined as

$$p = \frac{P}{K}, \quad q = \frac{KL^2}{\pi^2 B}. \quad (3)$$

When the rod is made up of a homogeneous material (and with uniform cross-section), the stiffness ratio reduces to $q = \lambda^2/\pi^2 \gtrsim 10^3$, where λ is the rod's slenderness. However, values of q below that range can be considered to model, via the extensible elastica, the mechanical response of architected one-dimensional structural elements. Although the identification of such structural elements falls outside the scope of the present research, a rough example is provided by a rectangular wire (die) helical spring, with a high cross section aspect-ratio. Moreover, by neglecting configurational forces [3, 8] (which do not influence bifurcation [7, 11]), another example is given by a round wire helical spring containing a coaxial flexible piston or a spring having one end sliding along a rod with uniform cross section.²

The bifurcation loads p for an extensible rod, subject to the above-mentioned boundary conditions, are reported in Fig. 2 (left part) at varying the stiffness ratio q . This result shows that bifurcation does not occur for $q < 8.183$, while two bifurcation loads (characterized by the same instability mode) exist

¹For simplicity the present analysis is developed under the assumption of linear axial behaviour. Although highly elastic materials such as rubber often display a nonlinear force/displacement behaviour, the linearity assumption introduced here strongly simplifies the treatment and is however adequate when the strain is not large or when the rod is realized via springs as the systems reported in Appendix A.

²The evaluation of the shear and axial stiffness of these structural examples is deferred to Appendix A.

under compression for $q > 8.183$. In the latter case, the two bifurcation loads have different mechanical interpretations: the one with smallest (greatest) absolute value is referred to as $p_{de}^{(-)}$ ($p_{re}^{(-)}$), because it is associated to destabilization (restabilization) of the trivial configuration at increasing compression. The structural system therefore displays a (single) restabilization.

Anticipating some of the results discussed in detail in section 3, the presence of a curved profile introduces a tensile instability [43, 6, 8] at the load value $p_{cr}^{(+)}$ and a double restabilization of the trivial configuration for $q \in (q_a, q_b)$, depending on the profile curvature. These features are shown on the right part of Fig. 2 for a profile with radius of curvature equal to 1/15 of the undeformed rod's length, for which the stiffness ratio range for double restabilization is defined by $q_a = 12.457$ and $q_b = 19.191$. The two bound values q_a and q_b will be shown to be approximately linearly increasing with the modulus of the dimensionless (negative) profile curvature at the origin, $f''(0)$.

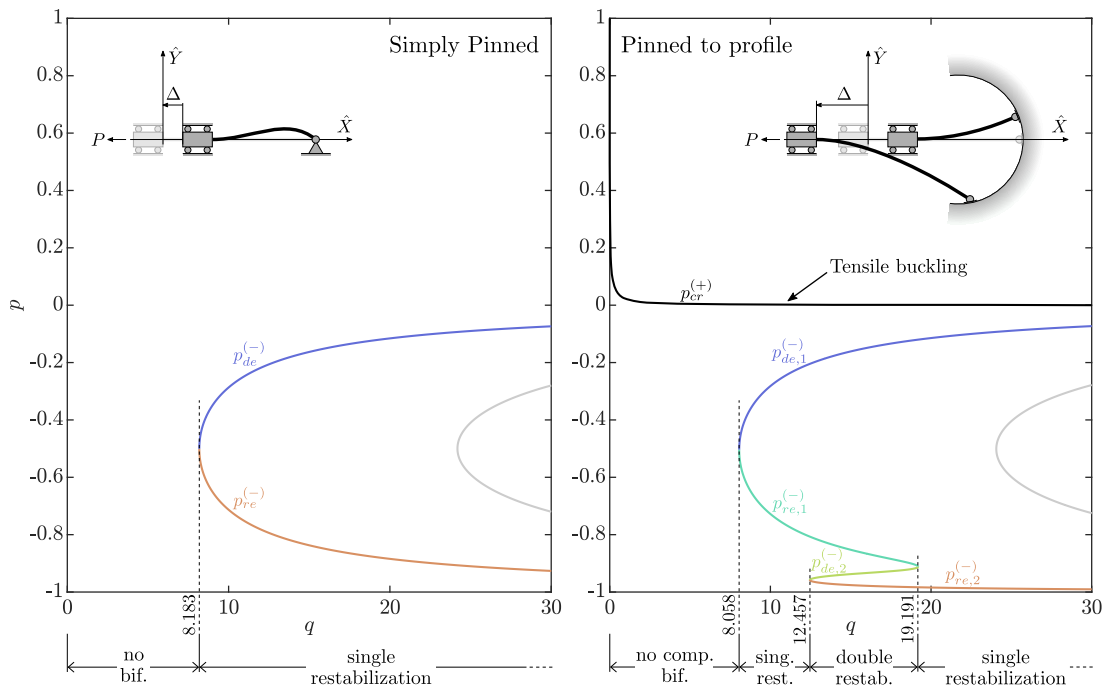


Figure 2: Bifurcation load p for an axially and flexurally deformable rod attached to a sliding clamp on its left end and pinned on the right end at a fixed point (left) or at a point constrained to move on a smooth curved profile (right, with a radius of curvature equal to 1/15 of the undeformed rod's length, $f''(0) = -15$). The bifurcation loads are reported at varying axial/bending stiffness ratio q . The tensile buckling load $p_{cr}^{(+)}$ is reported as black line, the compressive bifurcation loads of destabilization $p_{de}^{(-)}$ and restabilization $p_{re}^{(-)}$ associated to the first mode as coloured lines, while those of higher modes as gray lines. Ranges of stiffness ratio q for which single and double restabilization occurs are highlighted.

It is finally observed that the occurrence of the double restabilization requires a significant shortening of the structure, with the second (and final) restabilization displayed at a compressive deformation of more than 90% of the undeformed length. A spring, modelled as an extensional elastica, can be 'practically' used in order to achieve such a high compression experimentally. For example, 10 active coils with closed and ground ends of an helicoidal spring (with a wire diameter of 0.4 mm, and coil pitch of 10 mm) can achieve a shortening of more than 95% when compressed.

2 The extensible elastica with an end constrained to move along a frictionless profile

A soft rod is considered, connected to a sliding clamp on its left end, while the right end is constrained to move along a frictionless curved profile, Fig. 3. The rod has a straight undeformed configuration of

where d_X is the length of the elastica projection on the X -axis and d_Y is the vertical displacement of the pin on the right end of the rod

$$d_X(\varepsilon, \theta) = \int_0^L [1 + \varepsilon(\sigma)] \cos \theta(\sigma) d\sigma, \quad d_Y(\varepsilon, \theta) = \int_0^L [1 + \varepsilon(\sigma)] \sin \theta(\sigma) d\sigma. \quad (10)$$

The moving clamp is subject to the dead load P , positive when opposite to the X axis (namely, tensile state for the section at $S = 0$), and therefore the mechanical system is conservative. The potential energy \mathcal{V} of the structure is the sum of the axial and flexural elastic energies and the potential energy of the dead load,

$$\mathcal{V}(\varepsilon, \theta) = \frac{K}{2} \int_0^L [\varepsilon(\sigma)]^2 d\sigma + \frac{B}{2} \int_0^L [\theta'(\sigma)]^2 d\sigma - P \Delta, \quad (11)$$

where a prime stands for differentiation with respect to the relevant (spatial) argument. The first variation $\delta\mathcal{V}$ of the potential energy for perturbations in the strain $\delta\varepsilon$ and rotation $\delta\theta$ is given by

$$\delta\mathcal{V} = \int_0^L K \varepsilon(\sigma) \delta\varepsilon(\sigma) d\sigma - \int_0^L B \theta''(\sigma) \delta\theta(\sigma) d\sigma - P \delta\Delta, \quad (12)$$

where

$$\delta\Delta = \delta d_X - f' \left(\frac{d_Y}{L} \right) \delta d_Y, \quad (13)$$

$$\delta d_Y = \int_0^L [1 + \varepsilon(\sigma)] \cos \theta(\sigma) \delta\theta(\sigma) d\sigma + \int_0^L \sin \theta(\sigma) \delta\varepsilon(\sigma) d\sigma, \quad (14)$$

and

$$\delta d_X = - \int_0^L [1 + \varepsilon(\sigma)] \sin \theta(\sigma) \delta\theta(\sigma) d\sigma + \int_0^L \cos \theta(\sigma) \delta\varepsilon(\sigma) d\sigma. \quad (15)$$

The vanishing of the first variation $\delta\mathcal{V}$ for compatible perturbations $\delta\varepsilon$ and $\delta\theta$ provides the following coupled system of nonlinear equilibrium equations

$$\begin{aligned} B\theta''(S) - P [1 + \varepsilon(S)] \left[f' \left(\frac{d_Y}{L} \right) \cos \theta(S) + \sin \theta(S) \right] &= 0, \\ K\varepsilon(S) + P \left[f' \left(\frac{d_Y}{L} \right) \sin \theta(S) - \cos \theta(S) \right] &= 0, \end{aligned} \quad (16)$$

complemented by the algebraic constraint, Eq. (9), and the boundary conditions

$$Y(0) = 0, \quad \theta(0) = 0, \quad \theta'(L) = 0, \quad (17)$$

respectively prescribing the vanishing of the vertical displacement and of the rotation at the moving clamp, and the vanishing of the moment at the pin.

It should be noted that a reaction force R is realized at the pin on the profile. Due to the frictionless assumption, this force is orthogonal to the profile, and therefore inclined by the angle α with respect to the \hat{X} -axis given by the following condition

$$\alpha = \arctan \left[f' \left(\frac{d_Y}{L} \right) \right]. \quad (18)$$

The trivial straight configuration,

$$\theta(S) = 0, \quad \varepsilon(S) = \frac{P}{K}, \quad (19)$$

satisfies the equilibrium equations (16) if and only if $f'(0) = 0$. Henceforth, this profile property is assumed and under this circumstance bifurcation may be displayed depending on the dimensionless curvature of the profile at null \hat{Y} coordinate, $f''(0)$, and rod's properties (B , K , L) through the stiffness ratio q . As shown in [6], the profile shape can also be designed to present a discontinuous curvature at null \hat{Y} coordinate, $f''(0^+) \neq f''(0^-)$ (as in Fig. 3), to better tune the mechanical response under both signs of Δ (namely, both directions).

3 Bifurcation and stability of the trivial configuration

3.1 Bifurcation loads

Bifurcation conditions from the trivial straight configuration, Eq. (19), are investigated under small rotation $\theta(S)$ assumption, providing the linearized version of the equilibrium equations (16)

$$\begin{aligned} B\theta''(S) - P [1 + \varepsilon(S)] \left[\frac{d_Y}{L} f''(0) + \theta(S) \right] &= 0, \\ K\varepsilon(S) - P &= 0, \end{aligned} \quad (20)$$

where the following approximation is considered

$$f' \left(\frac{d_Y}{L} \right) \approx \frac{d_Y}{L} f''(0). \quad (21)$$

Eq. (20)₂ is automatically satisfied for the uniform axial strain field (19)₂ and Eq. (10)₂ can be linearized as

$$d_Y(\varepsilon, \theta) \approx \left(1 + \frac{P}{K} \right) \int_0^L \theta(\sigma) d\sigma. \quad (22)$$

By considering this latter approximation and the uniform axial strain field (19)₂ and by using the dimensionless load p and the (axial vs bending) stiffness ratio q , defined by Eq. (3), the equilibrium equation (20)₁ reduces to the following homogeneous and linear integro-differential equation

$$\theta''(S) - pq(1+p) \frac{\pi^2}{L^2} \left(\theta(S) + \frac{f''(0)}{L} (1+p) \int_0^L \theta(\sigma) d\sigma \right) = 0. \quad (23)$$

The basis for non-trivial solutions of $\theta(S)$ is found to be³

$$\theta(S) = \begin{cases} a \cos \left(\sqrt{-(1+p)pq} \frac{\pi S}{L} \right) + b \sin \left(\sqrt{-(1+p)pq} \frac{\pi S}{L} \right) + c, & p \in [-1, 0], \\ a \cosh \left(\sqrt{(p+1)pq} \frac{\pi S}{L} \right) + b \sinh \left(\sqrt{(p+1)pq} \frac{\pi S}{L} \right) + c, & p \in [0, \infty], \end{cases} \quad (24)$$

where a , b , and c are integration constants, where two of these can be computed as functions of the third one (which remains arbitrary, but small, in the present analysis) by imposing the boundary conditions.

Therefore, by substituting solutions (24) into equilibrium equation (23) and imposing the boundary conditions (17)₂ and (17)₃, a bifurcation with non-trivial equilibrium configuration exists when⁴

$$\begin{aligned} f''(0) \sqrt{-(1+p)pq} + pq\pi [1 + (1+p)f''(0)] \cot \left(\pi \sqrt{-(1+p)pq} \right) &= 0, & p \in [-1, 0], \\ f''(0) \sqrt{(1+p)pq} - pq\pi [1 + (1+p)f''(0)] \coth \left(\pi \sqrt{(1+p)pq} \right) &= 0, & p \in [0, \infty), \end{aligned} \quad (26)$$

defining the bifurcation load p as a function of the stiffness ratio q and dimensionless profile curvature at the origin $f''(0)$. It should be noted that the shape of the profile affects the bifurcation loads only

³The range $p < -1$ is excluded because it is representative of unphysical bifurcation, involving self-compensated rod configurations.

⁴In the inextensible limit ($K \rightarrow \infty$, $q \rightarrow \infty$, $p \rightarrow 0$, but $pq = PL^2/(\pi^2 B)$ remains finite), the bifurcation loads correspond to the solution of the following equations

$$\begin{aligned} f''(0) \sqrt{-pq} + pq\pi [1 + f''(0)] \cot(\pi \sqrt{-pq}) &= 0, & p < 0, \\ f''(0) \sqrt{pq} - pq\pi [1 + f''(0)] \coth(\pi \sqrt{pq}) &= 0, & p \geq 0. \end{aligned} \quad (25)$$

The latter equations are equivalent to that provided in [6] for the bifurcation loads (their Eq. (17) for $k = 0$). Here, the cases of positive and negative p , corresponding to tension and compression respectively, are separated in order to highlight the differences between the two. The separation also facilitates calculations because developments with imaginary values can be avoided.

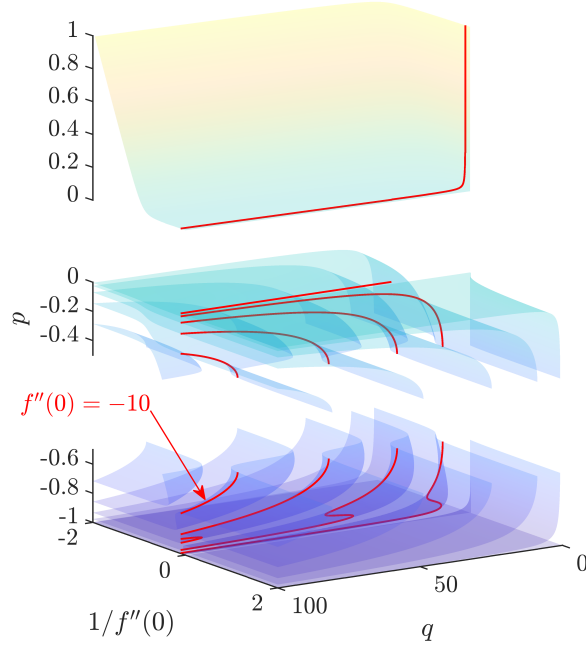


Figure 4: Isosurfaces of Eq. (26) showing the combination of stiffness ratio q , dimensionless radius of profile curvature at the origin $1/f''(0)$ and load p parameters for bifurcation. Note that all red curves belong to the same vertical plane defined by $1/f''(0) = -0.1$ and correspond to Fig. 5 (bottom, left). The representation of the lower surfaces has been slit to improve understanding.

because of its dimensionless curvature at the origin, $f''(0)$. These bifurcation conditions are displayed in Fig. 4 as surfaces in the three-dimensional space defined by the parameters p , q and $f''(0)$. Moreover, sections of these surfaces at constant values of $f''(0) = \{-10, -2, -0.5, 0.5, 2, 10\}$ are reported in Fig. 5.

From all of these representations, the following conclusions can be drawn.

- Differently from a standard Sturm-Liouville problem, governing bifurcation for an inextensible rod ($q \rightarrow \infty$), the number of bifurcation loads and modes becomes finite due to rod's extensibility. For instance, in Fig. 5 (upper part on the left) for stiffness ratio $q < 1.231$ there is only one mode in tension, while for $q \in (1.231, 9.264)$ there is only one mode in tension and only one in compression. Moreover, in Fig. 5 (upper part on the right) there is only one mode in compression for stiffness ratio $q \in (0.822, 8.836)$.
- Another effect related to the axial compressibility of the rod is that a bifurcation *mode* in compression corresponds to more than one bifurcation load. Indeed, except in the limit cases of coalescent loads (discussed below), the bifurcation loads in compression always occur *in pairs*, so that one corresponds to the *destabilization* (loss of stability) of the straight configuration, while the other to its *restabilization*. For instance, in Fig. 5 (upper part on the left) for $q > 1.231$ there is one bifurcation load for the first mode corresponding to the transition from stability to instability (at increasing compressive load) of the straight configuration. In addition, one restabilization load is found for the first mode, corresponding to the transition from instability to stability. Moreover, it can be observed in the same figure that for higher stiffness ratio q , where a plurality of modes emerge, the compressive bifurcation loads always occur in pairs.
- In tension: none or only one bifurcation load may exist, depending on the sign of the profile curvature at the origin $f''(0)$. The fact that only one critical load is found is related to the presence of the hyperbolic cotangent function in the bifurcation equation (26)₂. In particular:
 - for $f''(0) > 0$, tensile bifurcation does not occur, as in the inextensible case;

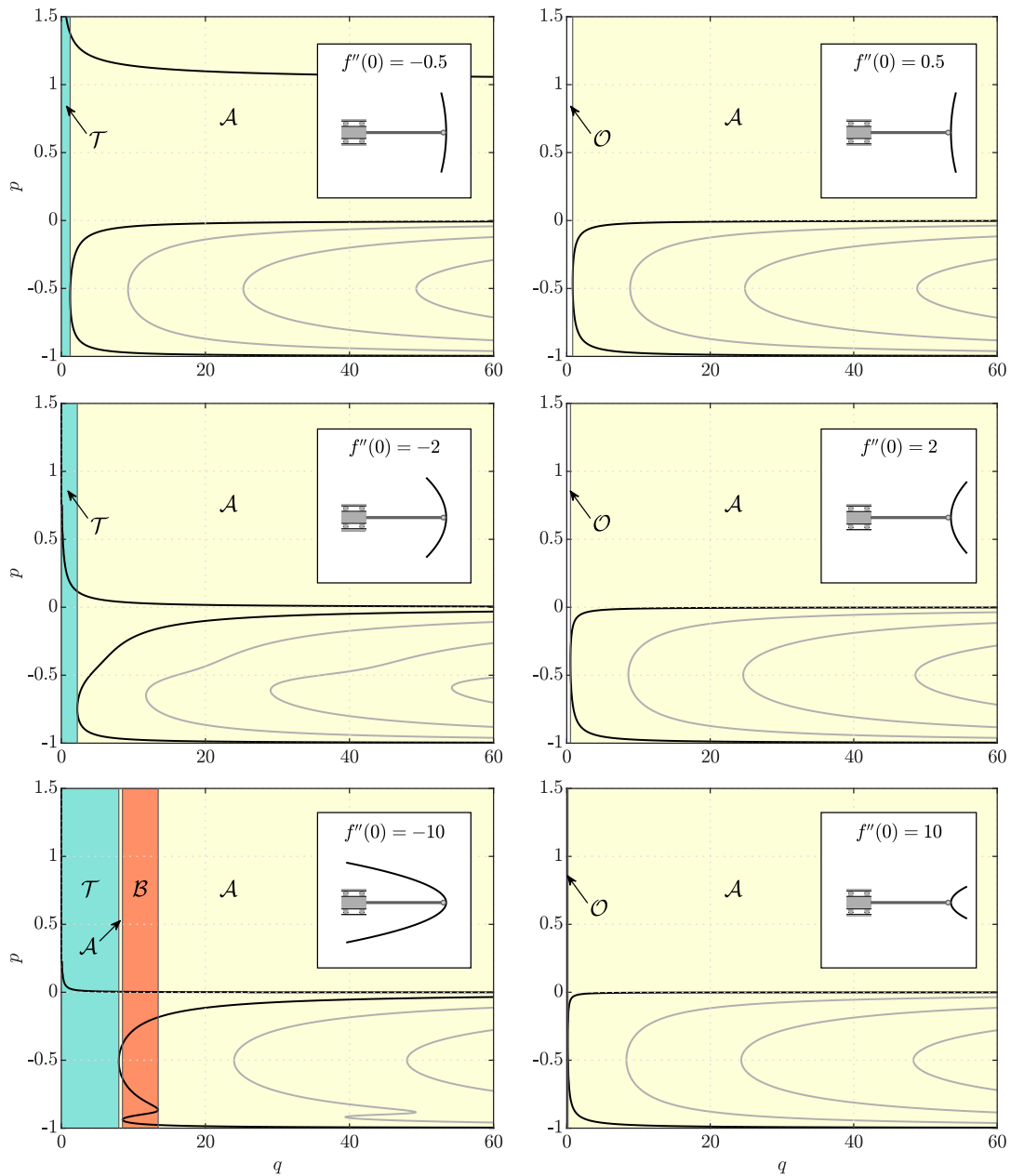


Figure 5: Tensile/compressive bifurcation load p as a function of q , for constant $f''(0) = \{-10, -2, -0.5, 0.5, 2, 10\}$. The regions \mathcal{O} , \mathcal{T} , \mathcal{A} , and \mathcal{B} are also shown. Tensile bifurcation does not occur for $f''(0) > 0$, but always occurs for $f''(0) < 0$. In compression, multiple bifurcation modes can be observed and their number depends of the values of q and $f''(0)$; considering here the first mode, there are regions where there are none (\mathcal{O} and \mathcal{T}), two (\mathcal{A}), and four (region \mathcal{B}) bifurcation compressive loads. The grey curves represent higher modes.

- for $f''(0) < 0$, one tensile bifurcation occurs at $p_{cr}^{(+)} > 0$ (where the superscript (+) reminds the reference to tensile load). This is in contrast with the inextensible case, where tensile bifurcation was existing in a more limited set, $f''(0) < -1$ [6].
- In compression: either bifurcation is excluded, or it may occur with 2 or 4 bifurcation loads associated to the same mode, depending on the values of q and $f''(0)$. More specifically, restricting attention only to the first compression mode, 2 main cases can be distinguished, differing in the number of bifurcations at varying q and $f''(0)$:
 - 2 bifurcation loads occur, associated to the first mode. Each of these corresponds to a destabilization load $(p_{de}^{(-)})$ and a restabilization load $(p_{re}^{(-)})$ (where the superscript (-) reminds the reference to compressive load),

$$-1 < p_{re}^{(-)} < p_{de}^{(-)} < 0. \quad (27)$$

An example of this behaviour is visible in Fig. 5 in the upper part on the left for $q > 1.231$;

- 4 bifurcation loads occur, associated to the first mode, corresponding to two pairs of destabilization/restabilization loads, $(p_{de,1}^{(-)}, p_{re,1}^{(-)})$ and $(p_{de,2}^{(-)}, p_{re,2}^{(-)})$, occurring in the following order⁵

$$-1 < p_{re,2}^{(-)} < p_{de,2}^{(-)} < p_{re,1}^{(-)} < p_{de,1}^{(-)} < 0. \quad (28)$$

An example of this behaviour is visible in Fig. 5 in the lower part on the left $q \in (8.488, 13.451)$;

- In compression: multiple bifurcation loads associated to the same mode may occur for modes higher than the first. An example is visible in Fig. 5 in the lower part on the left.

By considering all of the above described cases, four different subsets \mathcal{O} , \mathcal{T} , \mathcal{A} , and \mathcal{B} are distinguished in the $q - f''(0)$ plane (Fig. 6, upper part, on the left), differing in the number of the main bifurcation conditions as reported in Tab. 1.

Table 1: Numbers of main bifurcations for the subsets \mathcal{O} , \mathcal{T} , \mathcal{A} , and \mathcal{B} .

	Tensile bifurcation	Compressive bifurcation
\mathcal{O}	0	0
\mathcal{T}	1	0
\mathcal{A}	1	2 bif. loads associated with 1 st mode
\mathcal{B}	1	4 bif. loads associated with 1 st mode

In the following description of the bifurcation response, the terms ‘*destabilization*’ and ‘*restabilization*’ are introduced to respectively define a bifurcation load in compression representing a transition for the trivial configuration to become unstable or to return to being stable for compressive loads at increasing magnitude.

The $q - f''(0)$ pairs, defining the boundary of each subset, represent the transition in the bifurcation response. More specifically:

- the transition from subset \mathcal{A} to \mathcal{O} or \mathcal{T} corresponds to the transition from the presence of a destabilization $p_{de}^{(-)}$ and restabilization $p_{re}^{(-)}$ load (belonging to the subset \mathcal{A}) to a situation where bifurcation is excluded. This occurs at the coalescence

$$p_{de}^{(-)} = p_{re}^{(-)}; \quad (29)$$

⁵In the case when double restabilization may occur for a value of $f''(0)$, the nomenclature of the bifurcation loads $p_{de}^{(-)}$ and $p_{re}^{(-)}$ is enhanced by introducing a subscript 1 or 2 to distinguish between the first and second destabilization/restabilization loads. In order to simplify the presentation, this notation is preserved through a continuation principle for the roots passing from a set of q values where double restabilization is displayed to the set of single restabilization, as illustrated in Fig. 2.

- the transition from subset \mathcal{A} to \mathcal{B} correspond to the transition from a pair of bifurcation loads $(p_{de}^{(-)}, p_{re}^{(-)})$ to two pairs $(p_{de,1}^{(-)}, p_{re,1}^{(-)})$ and $(p_{de,2}^{(-)}, p_{re,2}^{(-)})$, all associated to the first bifurcation mode in compression. This necessarily involves one of the following coalescences

$$p_{de,1}^{(-)} = p_{re,1}^{(-)}, \quad \text{or} \quad p_{de,2}^{(-)} = p_{re,2}^{(-)}, \quad \text{or} \quad p_{de,2}^{(-)} = p_{re,1}^{(-)}. \quad (30)$$

Defining the range of $q \in (q_a, q_b)$ limiting the \mathcal{B} region, the bound values q_a and q_b are approximately linear in the dimensionless profile curvature when this takes large negative values,

$$q_a \approx 0.526 - 0.796f''(0), \quad q_b \approx 1.655 - 1.167f''(0), \quad \text{when } f''(0) < -10. \quad (31)$$

It is anticipated from Section 3.2 that, considering also tensile buckling (occurring at $p_{cr}^{(+)} \geq 0$), the set \mathcal{A} can be divided into two pairs of subsets, so that when the load p belongs to one pair the trivial configuration is stable, otherwise is unstable

$$\begin{aligned} \text{if } p \in (-1, p_{re}^{(-)}) \cup (p_{de}^{(-)}, p_{cr}^{(+)}) &\Rightarrow \text{trivial configuration is stable,} \\ \text{if } p \in (p_{re}^{(-)}, p_{de}^{(-)}) \cup (p_{cr}^{(+)}, \infty) &\Rightarrow \text{trivial configuration is unstable,} \end{aligned} \quad (32)$$

while the set \mathcal{B} can be divided into two triplets of subsets

$$\begin{aligned} \text{if } p \in (-1, p_{re,2}^{(-)}) \cup (p_{de,2}^{(-)}, p_{re,1}^{(-)}) \cup (p_{de,1}^{(-)}, p_{cr}^{(+)}) &\Rightarrow \text{stable trivial conf.,} \\ \text{if } p \in (p_{re,2}^{(-)}, p_{de,2}^{(-)}) \cup (p_{re,1}^{(-)}, p_{de,1}^{(-)}) \cup (p_{cr}^{(+)}, \infty) &\Rightarrow \text{unstable trivial conf.} \end{aligned} \quad (33)$$

The conditions of coalescence correspond to triplets of values for the parameters p , q , and $f''(0)$ and can be visualized as a curve in a three-dimensional parameter space. To investigate coalescence in a two-dimensional representation, Fig. 6 is introduced. In the upper part (on the left) of this figure, all transitions between the different sets \mathcal{O} , \mathcal{T} , \mathcal{A} , and \mathcal{B} are reported in the $q - f''(0)$ plane as curves drawn with different colours. The bifurcation load at which coalescence occurs is indicated with p^* and is reported in Fig. 6 at varying q (lower part, on the left) and at varying $f''(0)$ (upper part, on the right). Note that in the former case $f''(0)$ (in the latter case q) does not assume a fixed value, but varies.

A detail of the bifurcation p - q curves at fixed $f''(0) = \{-6, -15\}$ is reported in the lower part (on the right) of Fig. 6. Here, occurrences of coalescence $p = p^*$ are marked with diamonds of the same colour as the corresponding transition curve.

A comparison is presented in Fig. 7 between bifurcations calculated with two models of elastic rod, namely, an inextensible Euler-Bernoulli rod, and the axially deformable rod investigated in this article, both characterized by the same bending stiffness B and the latter investigated for constant values of $q = \{0.5, 10, 400\}$.

The comparison is reported in terms of a dimensionless value of the axial load P , namely, $pq = PL^2/(\pi^2 B)$, reported as a function of the dimensionless radius of profile curvature at the origin $1/f''(0)$.

Note in the figure that: (i.) tensile and compressive loads are considered; (ii.) some modes higher than the first are included (in light colour); (iii.) the response of the inextensible (extensible) model is reported with a dashed (continuous) line; (iv.) the region $p < -1$, highlighted though a gray background, should not be considered as the related compression level has no physical meaning.

From this figure, two main conclusions can be drawn:

- as the stiffness ratio q increases (from left to right in the figure), the bifurcation behaviour of the extensible rod converges to that pertaining to the inextensible one;
- in the figure on the left both models show a transition from a tensile to a compressive bifurcation load (the latter terminates when $p = -1$) and other bifurcation modes are not available. Even in both figures pertaining to $q = 10$ and 400 , and for both rod models, a tensile bifurcation load becomes compressive at the point $1/f''(0) = 0$. However, defined as the smaller (in absolute value) load, the critical load evidences a jump at this point, because the continuation of the tensile critical load prevails on a higher-order mode, which is critical for $1/f''(0) < 0$.

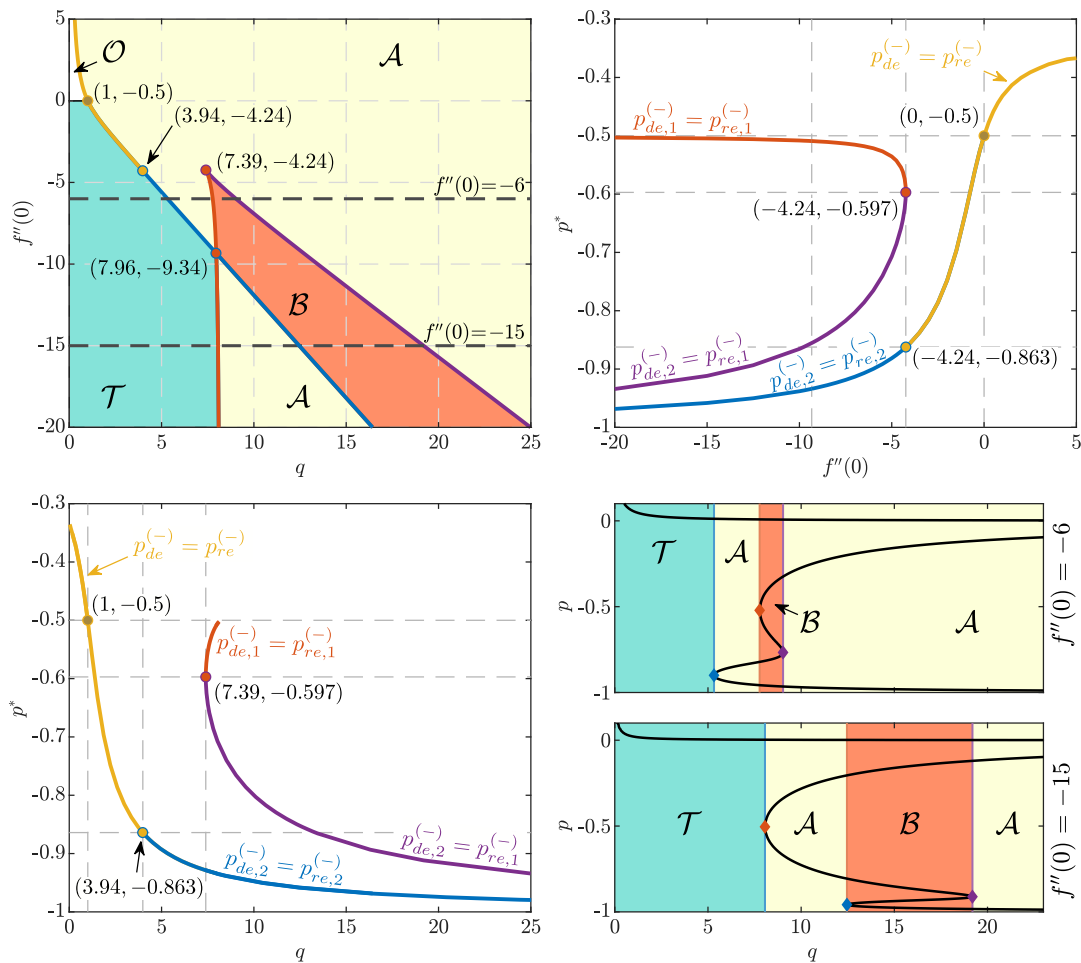


Figure 6: Upper part, left: Sets \mathcal{O} , \mathcal{T} , \mathcal{A} , and \mathcal{B} defined by the number of critical loads in compression (restricted to first mode) and in tension, as described in Table 1. Upper part, right and lower part, left: Coalescent bifurcation load p^* as a function of q (left, lower part) and of $f''(0)$ (right, upper part), defining the different boundaries between two of the sets \mathcal{O} , \mathcal{T} , \mathcal{A} , and \mathcal{B} . Lower part, right: Bifurcation load p versus q , evaluated for two values of $f''(0)$; here p^* is marked with a diamond of the same colour as the corresponding transition curve.

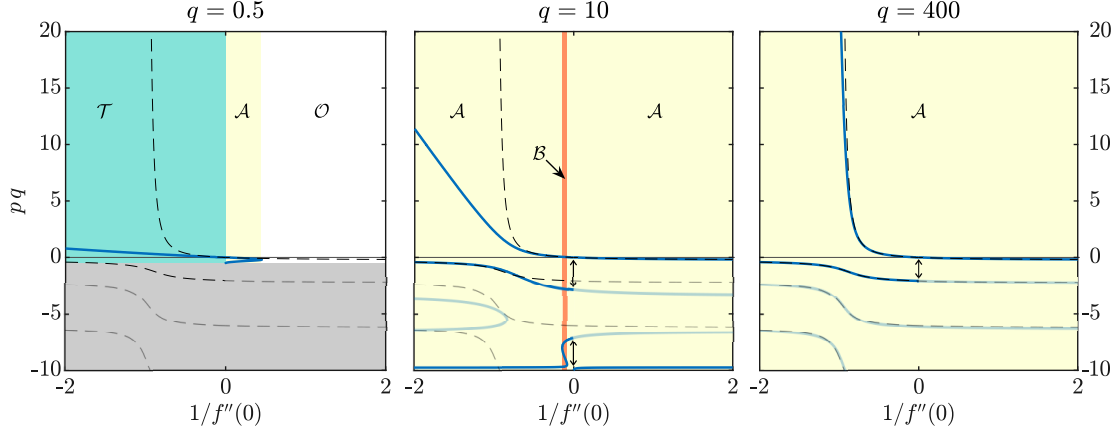


Figure 7: Comparison between tensile/compressive bifurcation loads $pq = PL^2/(\pi^2 B)$ for extensible (dashed lines) and inextensible (continuous lines) rod models and for $q = \{0.5, 10, 400\}$. The region shaded in gray corresponds to $p < -1$, which has no mechanical meaning. Bifurcation loads corresponding to modes higher than the first are drawn with lighter lines. As the stiffness ratio q increases, the bifurcation models converge. At the transition point $1/f''(0) = 0$ tensile instability turns to compressive and the critical load suffers a jump.

For completeness, the regions \mathcal{O} , \mathcal{T} , \mathcal{A} , and \mathcal{B} are also shown in Fig. 7 and these regions suggest the following observations.

- The compressive critical load $p_{de}^{(-)}$ for positive profile curvature $f''(0) = f''_a$ is bounded as follows (Fig. 6)

$$p_{de}^{(-)}(f''_a, q) \in \left[-\frac{1}{2}, 0\right], \quad \forall f''_a > 0. \quad (34)$$

- With reference to two values f''_a and f''_b of profile curvature at the origin $f''(0)$, the following inequalities hold for the critical loads in tension (Fig. 7)

$$f''_a < 0 \quad \text{and} \quad f''_a < f''_b \quad \Leftrightarrow \quad p_{cr}^{(+)}(f''_a, q) \leq p_{cr}^{(+)}(f''_b, q), \quad \forall q > 0, \quad (35)$$

and in compression

$$f''_a < f''_b \quad \Rightarrow \quad p_{de,1}^{(-)}(f''_a, q) < p_{de,1}^{(-)}(f''_b, q), \quad (36)$$

where the definition of critical loads is extended to include cases in which bifurcation does not occur, by assuming $p_{cr}^{(+)}(f'', q) = +\infty$ for $\{f'', q\} \in \mathcal{O}$ and $p_{de,1}^{(-)}(f'', q) = -\infty$ for $\{f'', q\} \in \mathcal{O} \cup \mathcal{T}$.

Asymptotic expressions for the bifurcation loads in the limit of vanishing profile curvatures, $f''(0) \rightarrow 0^\pm$, are reported in Appendix B.

Profile with curvature discontinuity at the origin. When the profile possesses a curvature discontinuity at the origin, $f''(0^+) \neq f''(0^-)$, each part of the profile defines its ‘own’ critical loads in tension $p_{cr}^{(+)}(f''(0^\pm), q)$ and in compression $p_{de}^{(-)}(f''(0^\pm), q)$. The tensile (compressive) critical load for the structure corresponds to the smallest (the highest) load,

$$\begin{aligned} p_{cr}^{(+)} &= \min \left[p_{cr}^{(+)}(f''(0^+), q), p_{cr}^{(+)}(f''(0^-), q) \right] > 0, \\ p_{cr}^{(-)} &= \max \left[p_{de,1}^{(-)}(f''(0^+), q), p_{de,1}^{(-)}(f''(0^-), q) \right] < 0. \end{aligned} \quad (37)$$

With the above premise, the design proposed in this article for the profile is based on the following two requirements.

- The first design requirement is a prescription that the shape of the profile that leads to a postcritical behaviour in tension and in compression is of the type illustrated in Fig. 3, so that in tension $p_{cr}^{(+)} = p_{cr}^{(+)}(f''(0^-), q)$ and in compression $p_{cr}^{(-)} = p_{de,1}^{(-)}(f''(0^+), q)$. From a kinematical point of view, this requirement is equivalent to the prescription that bifurcation under compression occurs with $d_Y > 0$ and under tension with $d_Y < 0$. When these conditions prevail, the following inequality holds

$$\Delta(p) d_Y(p) \leq 0, \quad (38)$$

and the critical loads (37) become only functions of $f''(0)$ and q

$$p_{cr}^{(+)} = p_{cr}^{(+)}(f''(0^-), q), \quad p_{cr}^{(-)} = p_{cr}^{(-)}(f''(0^+), q). \quad (39)$$

- The second design requirement is that the values of the two critical loads $p_{cr}^{(+)}$ and $p_{cr}^{(-)}$ must be assigned as desired.

It is clear that the inequality (38) imposes a restriction on the possibility to arbitrarily assign the two critical loads. This restriction can be obtained as follows.

After the loads are assigned, it can be proven that a specific value of q exists, say, \bar{q} , for which the critical loads are obtained with the same profile curvature at the origin, $f''(0^-) = f''(0^+)$, say, \bar{f}'' .

For $q \geq \bar{q}$ the inequality (38) fails, because

$$q > \bar{q} \implies f''(0^+) > f''(0^-) \quad \text{and} \quad p_{de,1}^{(-)}(f''(0^-)) > p_{de,1}^{(-)}(f''(0^+)) \quad (40)$$

meaning that the rod buckles in compression ($p < 0$) with $d_Y < 0$, oppositely to what is assumed through the inequality (38). More specifically, for given values of $p_{cr}^{(+)}$ and $p_{cr}^{(-)}$, the pairs $\{f'', \bar{q}\}$ define the range of values of $f''(0^+)$, $f''(0^-)$ and q for which Eq. (38) holds as

$$f''(0^-) \leq \bar{f}'' \leq 0 \leq f''(0^+), \quad q \leq \bar{q}. \quad (41)$$

Introducing the ratio $A = -p_{cr}^{(+)}/p_{cr}^{(-)}$, the parametric curves $\{\bar{f}''(p_{cr}^{(-)}, A), \bar{q}(p_{cr}^{(-)}, A)\}$ are reported in Fig. 8. The points at the intersection between a (dashed) curve pertaining to a value of $p_{cr}^{(-)}$ and a (coloured, solid) curve representative of a value of A lead the values of the pair \bar{f}'' and \bar{q} reported on the axes. Note that inside the gray zone in the figure bifurcation is excluded. The boundary of this zone corresponds to the occurrence of coalescent bifurcation loads $p_{cr}^{(-)} = p^*$.

3.2 Stability of the straight configuration from small amplitude vibration analysis

The stability of the straight configuration can be assessed by analysing the nature of the frequency of the time-harmonic small amplitude vibrations around the straight configuration. In particular, the presence (or absence) of non-real eigenfrequencies defines the instability (or stability) of the straight configuration, and the limit case of vanishing eigenfrequency would confirm the critical loads obtained from the quasi-static analysis performed in Sect. 3.1. With the purpose of studying the dynamic response of the system, a linear mass density γ is considered for the rod, so that the Lagrangian \mathcal{L} of the system can be written as

$$\begin{aligned} \mathcal{L} = & \int_0^L \frac{\gamma}{2} \left(\dot{\hat{X}}^2 + \dot{\hat{Y}}^2 \right) dS - \int_0^L \frac{B}{2} (\theta')^2 dS - \int_0^L \frac{K}{2} \varepsilon^2 dS - \int_0^L N_X \left\{ \hat{X}' - (1 + \varepsilon) \cos \theta \right\} dS \\ & - \int_0^L N_Y \left\{ \hat{Y}' - (1 + \varepsilon) \sin \theta \right\} dS - P \hat{X}(0) + R_X \left\{ \hat{X}(L) - L \left[f \left(\frac{\hat{Y}(L)}{L} \right) \right] \right\}, \end{aligned} \quad (42)$$

where N_X , N_Y , and R_X are Lagrangian multipliers (the first two representing the X and Y components of the internal force, the last representing the X component of the reaction R at the pin on the curved profile) and the dot over the functions stands for differentiation with respect to the time variable t . The

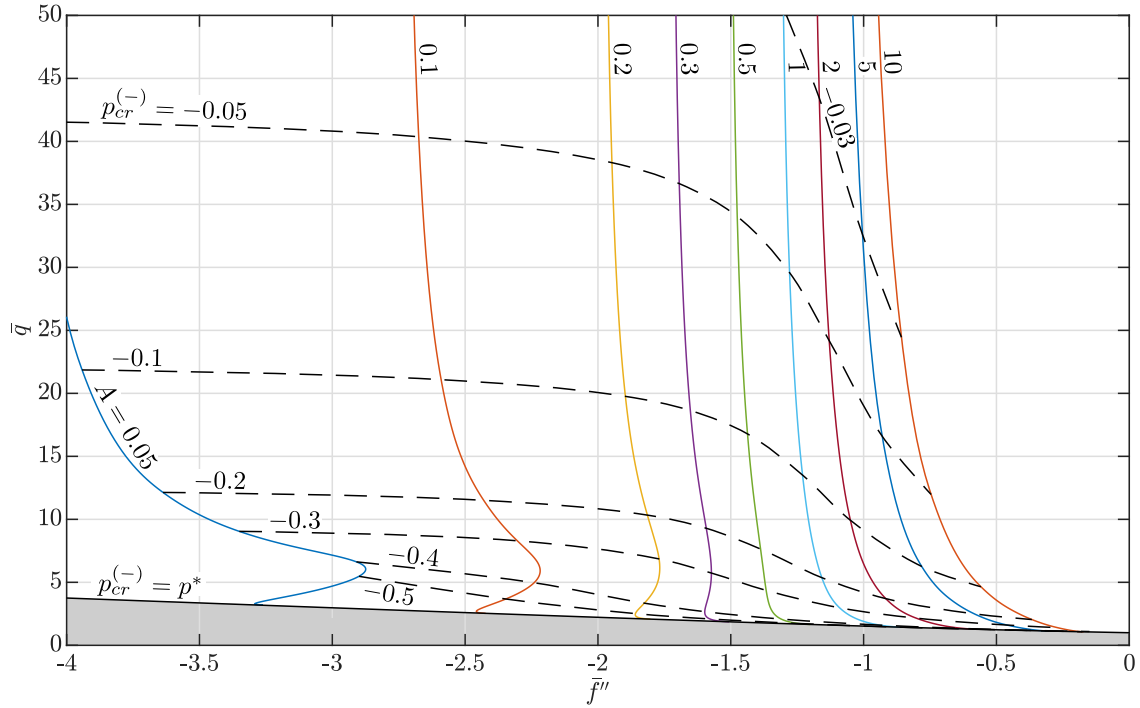


Figure 8: Parametric representation of profile curvature at the origin \bar{f}'' and stiffness ratio \bar{q} defining the limit parameters for which the two critical loads can be tuned separately. The intersection between (solid and coloured) curves at different $A = -p_{cr}^{(+)} / p_{cr}^{(-)}$ and (dashed) curves pertaining to $p_{cr}^{(-)}$ defines the corresponding pair (\bar{f}'', \bar{q}) . In the gray zone compressive bifurcation does not occur and its boundary corresponds to coalescent bifurcation loads $p_{cr}^{(-)} = p^*$.

equations of motion can be derived from the principle of least action as

$$\begin{aligned} N'_X &= \gamma \ddot{\hat{X}}, \\ N'_Y &= \gamma \ddot{\hat{Y}}, \\ B\theta'' - (1 + \varepsilon)[N_X \sin \theta - N_Y \cos \theta] &= 0, \\ K\varepsilon - N_X \cos \theta - N_Y \sin \theta &= 0, \end{aligned} \tag{43}$$

along with the boundary conditions

$$N_X(0) = P, \quad N_X(L) = R_X, \quad N_Y(L) = R_X f' \left(\frac{\hat{Y}(L)}{L} \right). \tag{44}$$

Considering small time-harmonic vibrations [10] around the trivial equilibrium configuration (19), the relevant fields are assumed through the method of separation of variables as

$$\begin{aligned} \hat{X}(S, t) &= S + \frac{P}{K}(S - L) + \bar{X}(S) e^{i\omega_x t}, & \hat{Y}(S, t) &= \bar{Y}(S) e^{i\omega_y t}, \\ \varepsilon(S, t) &= \frac{P}{K} + \bar{\varepsilon}(S) e^{i\omega_x t}, & \theta(S, t) &= \bar{\theta}(S) e^{i\omega_y t}, \\ N_X(S, t) &= P + \bar{N}_X(S) e^{i\omega_x t}, & N_Y(S, t) &= \bar{N}_Y(S) e^{i\omega_y t}, \\ R_X(t) &= P + \bar{R}_X e^{i\omega_x t}, \end{aligned} \tag{45}$$

where ω_x and ω_y are the circular frequencies for axial and flexural vibrations, respectively, and functions with an overbar denote functions of the spatial variable only. The amplitudes of the overbar functions

are considered to be driven by a small positive parameter η , so that

$$|\bar{X}| \approx |\bar{Y}| \approx |\bar{\varepsilon}| \approx |\bar{\theta}| \approx |\bar{N}_X| \approx |\bar{N}_Y| \approx |\bar{R}_X| \approx \eta, \quad \eta \gg \eta^2. \quad (46)$$

A substitution of the above expressions into Eqs. (43) and (44), by neglecting higher-order terms in η , yields the following decoupled differential equations in the axial and transverse amplitude oscillations

$$\begin{aligned} \bar{X}''(S) + \hat{\omega}_x^2 \frac{\pi^2}{L^2} \bar{X}(S) &= 0, \\ \bar{Y}^{(iv)}(S) - (1+p)pq \frac{\pi^2}{L^2} \bar{Y}''(S) - (1+p)^2 \hat{\omega}_y^2 \frac{\pi^4}{L^4} \bar{Y}(S) &= 0, \end{aligned} \quad (47)$$

where

$$\hat{\omega}_x^2 = \frac{\gamma \omega_x^2 L^2}{\pi^2 K}, \quad \hat{\omega}_y^2 = \frac{\gamma \omega_y^2 L^4}{\pi^4 B}, \quad (48)$$

to be complemented with the boundary conditions⁶

$$\bar{X}'(0) = 0, \quad \bar{X}(L) = 0, \quad (51)$$

for axial oscillations, and

$$\begin{aligned} \bar{Y}(0) = \bar{Y}'(0) = \bar{Y}''(L) &= 0, \\ \bar{Y}'''(L) - (1+p)pq \frac{\pi^2}{L^2} \left[\bar{Y}'(L) + (1+p) \frac{f''(0)}{L} \bar{Y}(L) \right] &= 0, \end{aligned} \quad (52)$$

for transverse ones. Due to motion decoupling from Eqs. (47), ω_x and ω_y are independent from each other. Taking into account the boundary conditions (51), the integration of Eq. (47)₁ provides the axial mode as

$$\bar{X}(S) = \cos\left(\frac{\pi \hat{\omega}_x S}{L}\right), \quad (53)$$

where

$$\hat{\omega}_x = n - \frac{1}{2}, \quad n \in \mathbb{N}, \quad (54)$$

showing that the axial vibrations have always real circular frequencies ω_x . The transverse mode can be obtained from integration of Eq. (47)₂ as

$$\bar{Y}(S) = C_1 \cos\left(\frac{\pi \lambda_1 S}{L}\right) + C_2 \cos\left(\frac{\pi \lambda_2 S}{L}\right) + C_3 \sin\left(\frac{\pi \lambda_1 S}{L}\right) + C_4 \sin\left(\frac{\pi \lambda_2 S}{L}\right), \quad (55)$$

where

$$\lambda_{1,2} = \sqrt{\frac{1+p}{2}} \sqrt{-pq \pm \sqrt{(pq)^2 + 4\hat{\omega}_y^2}}, \quad (56)$$

and C_1 , C_2 , C_3 , and C_4 are the coefficients defining the transverse shape. The homogeneous linear problem in the coefficients C_j ($j = 1, \dots, 4$), obtained by imposing the boundary conditions (52) to the transverse shape, Eq. (55), represents an eigenvalue problem where $\hat{\omega}_y^2$ is the eigenvalue and the coefficients C_j define the eigenvector. In the present problem, it is found that an infinite set of $\hat{\omega}_y^2$ values exists, where each value is related to a specific transverse mode, and that these values are real numbers. Therefore, it can be concluded that:

⁶The expansion of Eq. (8) truncated to linear terms in $\hat{Y}(L)$ is

$$\hat{X}(L) = Lf(0) + f'(0)\hat{Y}(L), \quad (49)$$

which, under the considered assumption $f'(0) = 0$, reduces to

$$\hat{X}(L) = Lf(0), \quad (50)$$

implying the boundary condition (51)₂.

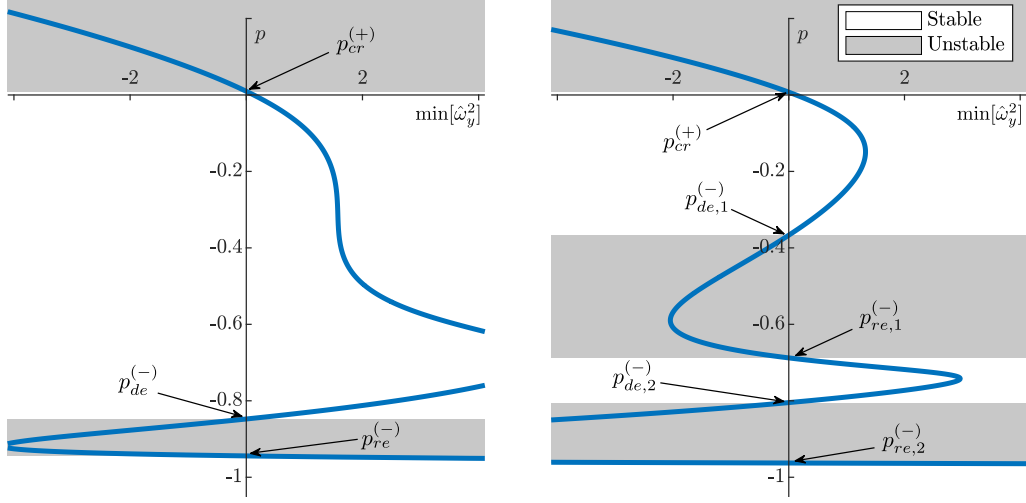


Figure 9: Smallest eigenvalue $\hat{\omega}_y^2 = \gamma \omega_y^2 L^4 / (\pi^4 B)$ for $f''(0) = -6$ when the dimensionless applied load p is varied. Two stiffness ratios are considered to analyse the stability in subset \mathcal{A} (left, $q = 6.5$) and subset \mathcal{B} (right, $q = 8.5$). Stability (or instability) of the straight configuration corresponds to positiveness (or negativeness) of the smallest eigenvalue $\hat{\omega}_y^2$. Restabilization (left) or double restabilization (right) is found.

- if the smallest eigenvalue $\hat{\omega}_y^2$ is positive ($\min[\hat{\omega}_y^2] > 0$), the trivial configuration is stable because all the eigenmodes have real circular eigenfrequency ω_y ;
- if the smallest eigenvalue $\hat{\omega}_y^2$ is negative ($\min[\hat{\omega}_y^2] < 0$), the trivial configuration is unstable because at least one of the eigenmodes has an imaginary circular eigenfrequency ω_y (corresponding to a divergent oscillation);
- if one of the eigenvalues $\hat{\omega}_y^2$ vanishes, the trivial configuration is at the transition between the two previous cases for the specific eigenmode. This condition is the dynamic counterpart of the previously analysed bifurcation for quasi-static deformation.⁷

As example, the smallest eigenvalue $\hat{\omega}_y^2$ is reported as a function of the dimensionless load p in Fig. 9, for $f''(0) = -6$ and two different stiffness ratios, $q = 6.5$ (left) and $q = 8.5$ (right), representative of sets \mathcal{A} and \mathcal{B} , respectively. Load ranges realizing stable (unstable) trivial configuration, and corresponding to positive (negative) smallest eigenvalue $\hat{\omega}_y^2$, are highlighted as white (gray) regions. These plots confirm the dimensionless load ranges corresponding to stable and unstable straight configuration as expressed by Eq. (32) for set \mathcal{A} and by Eq. (33) for \mathcal{B} , and the associated restabilization and double-restabilization phenomena.

4 Analytical solution for the nonlinear kinematics of the structure

As the rotation and deformation may reach large values in the post-critical response, the nonlinear problem defined by Eq. (16) is investigated as two decoupled problems. The first is the underlying problem of the deformation of the extensible elastica, while the second is the satisfaction of the boundary condition for the right end that is constrained by the curved profile.

For the extensible elastica, the closed-form solution for a cantilever beam with a force imposed at the free end provided in [4] is exploited. In particular, this solution, based on Jacobi elliptic functions as an improvement over the elliptic integral approaches considered before [18, 19, 26, 28, 34], is specialized to impose the constraint expressed by Eq. (9).

⁷The equation of motion (47)₂, in the case when $\hat{\omega}_y^2 = 0$, is equivalent to the bifurcation equation (23), obtained for quasi-static deformation. These two just differ in the reference kinematic field, corresponding to $\hat{Y}(S)$ in dynamics and $\theta(S)$ for quasi-static deformation. These are related to each other through $\hat{Y}'(S) = (1 + p)\theta(S)$ under the small rotation assumption.

4.1 General solution for a cantilever beam with a force imposed at its end

The closed-form solution for a cantilever beam with a concentrated load at the free end has been derived by Batista [4]. This solution is exploited here in the case of unshearable rod (parameter $\nu = 1$ in [4]) and by considering that the concentrated load is provided by the reaction force of the profile, having magnitude $R > 0$ and inclination $\alpha \in [-\pi, \pi]$ as reported in Fig. 3.

Introducing the following non-dimensional parameters⁸

$$\rho^2 = \frac{RL}{B}, \quad \lambda = L\sqrt{\frac{K}{B}}, \quad \hat{S} = \frac{S}{L}, \quad (57)$$

the rotation $\theta(S)$ and strain $\varepsilon(S)$ fields are given by

$$\theta(S) = 2 \arcsin \left[k \frac{\operatorname{sn}(\tilde{\rho}\hat{S} + C, \tilde{k})}{\sqrt{1 + m^2 \operatorname{cn}^2(\tilde{\rho}\hat{S} + C, \tilde{k})}} \right] - \alpha, \quad \varepsilon(S) = -\frac{\rho^2}{\lambda^2} \cos(\theta(S) + \alpha), \quad (58)$$

where

$$m^2 = \frac{\rho^2 k^2}{\lambda^2 (1 - \rho^2(1 - k^2))}, \quad \tilde{\rho} = \rho \sqrt{1 + \frac{\rho^2(2k^2 - 1)}{\lambda^2}}, \quad \tilde{k}^2 = \frac{k^2 + m^2}{1 + m^2}. \quad (59)$$

The integration of the kinematic fields (58)₁ through Eq. (6) provides the position of the rod, in the rotated reference frame, at the curvilinear coordinate S as

$$\begin{aligned} x(S) &= \frac{2\tilde{\rho}}{\rho^2} \left\{ \left(\frac{E(\tilde{k})}{K(\tilde{k})} - \frac{1}{2} \right) \tilde{\rho}\hat{S} + Z(\tilde{\rho}\hat{S} + C, \tilde{k}) - Z(C, \tilde{k}) \right. \\ &\quad \left. - m^2 \left[\frac{\operatorname{sn}(\tilde{\rho}\hat{S} + C, \tilde{k}) \operatorname{cn}(\tilde{\rho}\hat{S} + C, \tilde{k}) \operatorname{dn}(\tilde{\rho}\hat{S} + C, \tilde{k})}{1 + m^2 \operatorname{cn}^2(\tilde{\rho}\hat{S} + C, \tilde{k})} - \frac{\operatorname{sn}(C, \tilde{k}) \operatorname{cn}(C, \tilde{k}) \operatorname{dn}(C, \tilde{k})}{1 + m^2 \operatorname{cn}^2(C, \tilde{k})} \right] \right\} L, \quad (60) \\ y(S) &= \frac{2k\tilde{\rho}\sqrt{1+m^2}}{\rho^2} \left[\frac{\operatorname{cn}(C, \tilde{k})}{1 + m^2 \operatorname{cn}^2(C, \tilde{k})} - \frac{\operatorname{cn}(\tilde{\rho}\hat{S} + C, \tilde{k})}{1 + m^2 \operatorname{cn}^2(\tilde{\rho}\hat{S} + C, \tilde{k})} \right] L, \end{aligned}$$

while the rod's curvature $\kappa(S) = \theta'(S)$ follows as

$$\kappa(S) = \frac{1}{L} \frac{2\tilde{\rho}k\sqrt{1+m^2} \operatorname{cn}(\tilde{\rho}\hat{S} + C, \tilde{k})}{1 + m^2 \operatorname{cn}^2(\tilde{\rho}\hat{S} + C, \tilde{k})}. \quad (61)$$

In the above equations, K and E are the complete elliptic integrals of the first and second kind, Z , sn , cn , dn are Jacobi elliptic functions, and C is the constant of integration that can be found by imposing the boundary condition of zero bending moment, equivalent to null curvature, at the free end, $\theta'(L) = \kappa(L) = 0$.

From the boundary condition of null rotation at the clamp, $\theta(0) = 0$, the following equation is obtained

$$k \frac{\operatorname{sn}(C, \tilde{k})}{\sqrt{1 + m^2 \operatorname{cn}^2(C, \tilde{k})}} - \sin \frac{\alpha}{2} = 0, \quad (62)$$

to be solved for the value of k . The boundary condition at the right end $\kappa(L) = 0$ yields a formula for C

$$C = -\tilde{\rho} + (2n - 1)K(\tilde{k}), \quad n \in \mathbb{N}, \quad (63)$$

where n is the mode number. Once k is determined, the coordinates of the curve in the rotated reference frame $x - y$ can be evaluated from Eq. (60), and those in the reference frame $X - Y$, moving with the sliding clamp, follows as

$$X(S) = x(S) \cos \alpha + y(S) \sin \alpha, \quad Y(S) = -x(S) \sin \alpha + y(S) \cos \alpha. \quad (64)$$

⁸It should be noted that here the symbol ρ is used instead of ω used originally in [4] in order to not create confusion with the analogous symbols used to denote the angular frequencies in Sect. 3.2.

Finally, recalling from Eq. (10) that

$$X(L) = d_X, \quad Y(L) = d_Y, \quad (65)$$

these two quantities can be expressed as a respective function, \mathcal{G}_X and \mathcal{G}_Y (for conciseness not explicitly reported here), depending on the angle α and the reaction magnitude R ,

$$d_X = \mathcal{G}_X(\alpha, R), \quad d_Y = \mathcal{G}_Y(\alpha, R). \quad (66)$$

Because $\kappa(L) = 0$, the parameter k can be related with the rotation of the beam at the free end $\theta_L = \theta(L)$, by evaluating (58) at $S = L$, through the following formula

$$k = \sin \frac{\theta_L + \alpha}{2}. \quad (67)$$

4.2 Imposition of the curved profile constraint

The general solution for a cantilever beam recalled in the previous section is now considered as having unknown reaction force R and angle α . Because the load P is imposed at the sliding clamp, equilibrium implies the following relation between the angle $\alpha \in [-\pi, \pi]$ and the positive reaction force R

$$P = R \cos \alpha. \quad (68)$$

Due to the absence of friction, the reaction force R is perpendicular to the constraint profile, relating α with the vertical deflection of the free end of the cantilever beam d_Y as⁹

$$\alpha = \arctan \left(f' \left(\frac{d_Y}{L} \right) \right) + \frac{\pi}{2} [1 - \text{sgn}(P)]. \quad (69)$$

Considering Eq. (68), relation (66) can be rewritten as

$$d_X = \mathcal{G}_X \left(\alpha, \frac{P}{\cos \alpha} \right), \quad d_Y = \mathcal{G}_Y \left(\alpha, \frac{P}{\cos \alpha} \right), \quad (70)$$

and, since the angle α is related to d_Y through Eq. (69), Eq. (70)₂ provides a fixed-point recursive relation for the value of d_Y .

The nonlinear equilibrium configurations can be obtained by solving a reverse problem, where the displacement Δ is imposed while the load P is unknown. In this way, Eqs. (9), (70), and (62) provide a system of three nonlinear equations in the three unknown parameters P , θ_L , and d_Y to be solved for a given Δ value

$$\begin{cases} \mathcal{G}_X \left(\alpha, \frac{P}{\cos \alpha} \right) - L \left[1 + f \left(\frac{d_Y}{L} \right) \right] - \Delta = 0, \\ \mathcal{G}_Y \left(\alpha, \frac{P}{\cos \alpha} \right) - d_Y = 0, \\ k \frac{\text{sn}(C, \tilde{k})}{\sqrt{1 + m^2 \text{cn}^2(C, \tilde{k})}} - \sin \frac{\alpha}{2} = 0. \end{cases} \quad (71)$$

Due to the nonlinearity of system (71), none, one, or multiple non-trivial equilibrium configurations can be obtained for a given value of the end displacement Δ .

⁹The definition (69) for the angle α is introduced to ensure positiveness of the profile reaction, $R > 0$, independently from the sign of the applied load P . Moreover, the restriction $R > 0$ is also needed to exploit the solution obtained in [4].

4.3 Symmetric profile

Reference is made to a parabolic constraint profile (symmetric about the \widehat{X} -axis) and described by

$$f(\xi) = 1 + \frac{f''(0)}{2} \xi^2, \quad (72)$$

where $\xi = \widehat{Y}/L$.

The equilibrium paths in terms of load p as a function of the clamp displacement Δ/L , rotation θ_L , and vertical coordinate d_Y/L of the end of the rod are shown in Fig. 10 for $f''(0) = -10$. Two different values of q are considered, $q = 8.4$ and $q = 10$, corresponding to a single and a double restabilization, respectively. Stable and unstable configurations are distinguished through continuous and dotted lines, respectively.¹⁰ Restricting attention to non-trivial configurations, the force-displacement diagrams reveal one stable non-trivial configuration (highlighted with red lines) and, as a result, the system is bistable. Because none of the non-trivial bifurcation paths (highlighted with green dotted lines) is stable in compression, the loss of stability at these bifurcation points realizes a ‘snap’ motion towards the non-trivial stable configuration, as shown by the arrows in Fig. 10. Moreover, since $f''(0)$ is negative, a tensile bifurcation exists. The non-trivial path (highlighted with purple lines) at the tensile bifurcation is found to be stable.

4.4 Skew-symmetric profile with discontinuous curvature at the origin

A profile, skew-symmetric about the \widehat{X} -axis, is considered as

$$f(\xi) = 1 + \frac{f''(0^+)}{2} \xi |\xi|, \quad (73)$$

displaying a discontinuity in the profile curvature at the origin,

$$f''(0^-) = -f''(0^+). \quad (74)$$

For this system, attention is restricted only to the continuous stable path in terms of p q - Δ/L , reported in Fig. 11 for $q = \{4, 30\}$ and $f''(0^+) = \{2, 10\}$. It can be noted that, although the profile shape is skew-symmetric about the \widehat{X} -axis, the force-displacement curve does not evidence any symmetry, except along the trivial branch before bifurcation. In fact, the post-buckling behavior of the system depends not only on the constraint shape but also on the signs of the profile angle $f'(\xi)$ and curvature $f''(\xi)$.

5 Optimization of the profile shape for a design force-displacement curve

The developed theoretical framework is exploited here to design a device displaying a prescribed force-displacement p - Δ/L curve. The structure displays a linear elastic range, limited within the tensile/-compressive bifurcations, $p = \Delta/L \in [p_{cr}^{(-)}, p_{cr}^{(+)}]$, defined by Eq. (37). The design force-displacement curve is assumed to be characterized as

$$p\left(\frac{\Delta}{L}\right) = \begin{cases} \mathbf{p}^{(-)}\left(\frac{\Delta}{L}\right), & \frac{\Delta}{L} < p_{cr}^{(-)}, \\ \frac{\Delta}{L}, & \frac{\Delta}{L} \in [p_{cr}^{(-)}, p_{cr}^{(+)}], \\ \mathbf{p}^{(+)}\left(\frac{\Delta}{L}\right), & \frac{\Delta}{L} > p_{cr}^{(+)}, \end{cases} \quad (75)$$

where $\mathbf{p}^{(+)}(\Delta/L)$ and $\mathbf{p}^{(-)}(\Delta/L)$ define a target behaviour to be displayed after bifurcation, tensile and compressive, respectively, and satisfying the continuity condition

$$\mathbf{p}^{(\pm)}\left(p_{cr}^{(\pm)}\right) = p_{cr}^{(\pm)}. \quad (76)$$

¹⁰Stability character of the non-trivial configurations and snap motion towards them have been assessed through the numerical solution of the nonlinear dynamic equations (43) and (44).

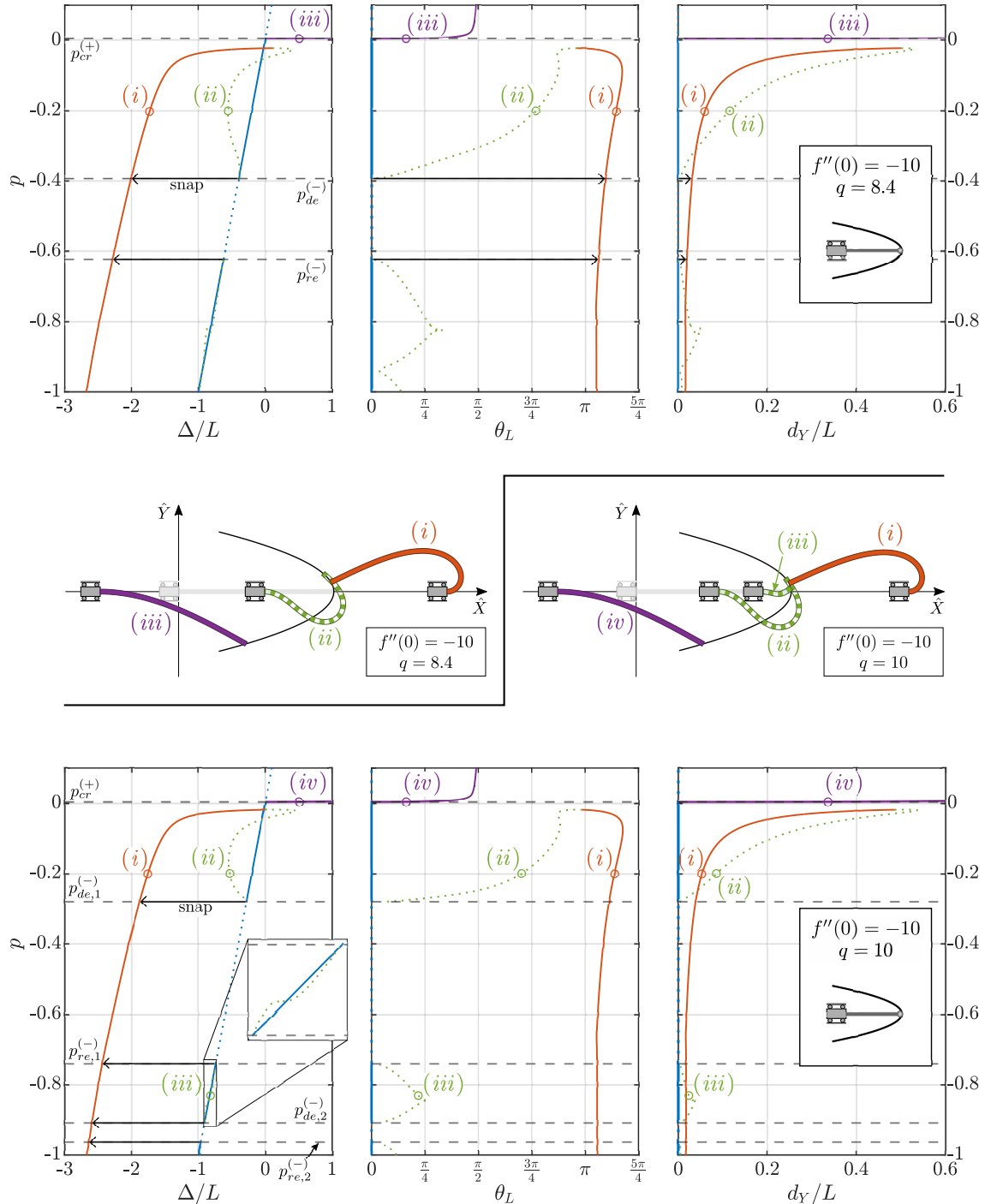


Figure 10: Post-critical behaviour in terms of dimensionless force p versus different measures of structural deformation: clamp displacement Δ , right end rotation θ_L and vertical displacement d_Y . $f''(0) = -10$ and $q = 8.4$ (upper part) and $q = 10$ (lower part). Some stable and unstable deformed configurations are shown for specific non-trivial states in the central part.

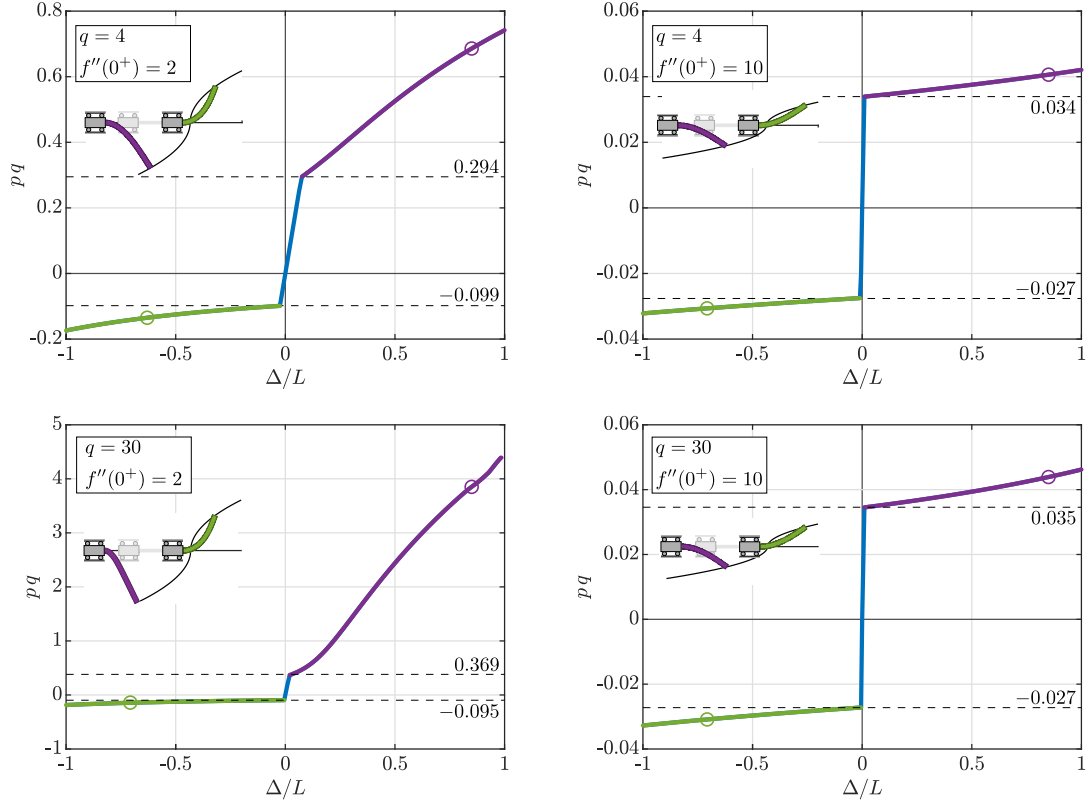


Figure 11: Force ($pq = PL^2/(\pi^2 B)$) – displacement (Δ/L) diagram for a structure with $q = 4, 30$ and skew-symmetric profile defined by Eq. (73) with $f''(0^+) = 2$ (left) and $f''(0^+) = 10$ (right). The deformed shapes shown in the inset correspond to the pq - Δ/L pairs highlighted with a circle (with corresponding colour) on the non-trivial path.

Considering that the two critical values are independent of each other, a discontinuous profile curvature at the origin is needed to control independently these two thresholds as related to the tensile and compressive loading branches of the structure. As previously shown, the stiffness ratio q and two profile curvatures at the origin $f''(0^-)$ and $f''(0^+)$ have to lie within the ranges provided by Eq. (41).

The post-buckling displacement Δ is discretized in the two sets $\Delta_i^{(\pm)}$, characterized by $N^{(\pm)}$ discretization points ($i = 0, \dots, N^{(\pm)}$), satisfying

$$\Delta_0^{(\pm)} = p_{cr}^{\pm} L, \quad \left| \Delta_{i+1}^{(\pm)} \right| > \left| \Delta_i^{(\pm)} \right|, \quad \pm \Delta_i^{(\pm)} > 0. \quad (77)$$

Considering the profile as the union of two parts differing in the sign of Y , the dimensionless coordinate Y/L is discretized through the unknown points $\xi_i^{(\pm)}$, corresponding to $\Delta_i^{(\pm)}$, where

$$\xi_0^{(\pm)} = 0^{\pm}, \quad \left| \xi_{i+1}^{(\pm)} \right| > \left| \xi_i^{(\pm)} \right|, \quad \pm \xi_i^{(\pm)} > 0. \quad (78)$$

The profile shape is discretized as

$$f(\xi) = 1 + \frac{1}{2} \sum_{j=0}^{i-1} h_{j+1}^{(\pm)} \left(\xi_{j+1}^{(\pm)} - \xi_j^{(\pm)} \right)^2 + \frac{1}{2} h_{i+1}^{(\pm)} \left(\xi - \xi_i^{(\pm)} \right)^2, \quad \xi \in \left[\xi_i^{(\pm)}, \xi_{i+1}^{(\pm)} \right], \quad (79)$$

where $h_{i+1}^{(\pm)}$ is the piecewise constant profile curvature value,

$$f''(\xi) = h_{i+1}^{(\pm)}, \quad \xi \in \left(\xi_i^{(\pm)}, \xi_{i+1}^{(\pm)} \right), \quad (80)$$

In order to achieve the target force-displacement curve, a fitting loop is devised. The algorithm initiates with $i = 0$ and is repeated for increasing values of i . After selecting the stiffness ratio q of the rod, the generic unknown point $\xi_{i+1}^{(\pm)}$ and corresponding profile curvature value $h_{i+1}^{(\pm)}$ can be found through a solution of the nonlinear system (71) by imposing $\Delta_{i+1}^{(\pm)}$ and prescribing the force p in agreement with the target response, Eq. (75), as

$$p\left(\frac{\Delta_{i+1}^{(\pm)}}{L}; \xi_{i+1}^{(\pm)}, h_{i+1}^{(\pm)}\right) = \mathbf{p}^{(\pm)}\left(\frac{\Delta_{i+1}^{(\pm)}}{L}\right). \quad (81)$$

It is worth noting that the profile optimization can be unsuccessful at a specific value of Δ for the following issues.

Issue 1 – A too stiff response is requested. Indeed, the target force-displacement curve $\mathbf{p}^{(\pm)}(\Delta/L)$ has its first derivative bounded from above by the maximum post-critical stiffness ratio $k_{\max} \in (0, 1)$ as¹¹

$$\frac{d\mathbf{p}^{(\pm)}(\Delta/L)}{d(\Delta/L)} < k_{\max}(q, \hat{Y}), \quad (83)$$

because a unit value would correspond to the stiffest behaviour given by the purely axial state, which is instead weakened in the post-critical region by flexure. It is also observed that high values of q and \hat{Y} define small maximum post-critical stiffness ratio k_{\max} ;

Issue 2 – The elastica is unstable. Although a profile shape is found, the involved equilibrium configuration of the rod may become unstable. In particular, the stable/unstable response is affected by the prescribed boundary condition, namely, it may change whether displacement Δ or load p are imposed;

Issue 3 – A force reversal [6, 9, 11] is excluded. Because the profile shape is described via the horizontal coordinate \hat{X} through the function $f(\hat{Y}/L)$, Eq. (8), the present formulation cannot be exploited to realize force reversals (p changing sign at a given end displacement $\Delta \neq 0$). Therefore, the target response is subject to the following constraint

$$\pm \mathbf{p}^{(\pm)} > 0. \quad (84)$$

In the limit condition given by $p = 0$, the optimization procedure fails providing $f' \rightarrow \infty$, because the only possible equilibrium configuration is realized for a reaction inclination angle $\alpha = \pm\pi/2$.

While the first two issues above are inherent to the considered model and cannot be avoided, the latter restriction can be overcome through a parametric planar description of the profile curve, as for example describing the profile as $\hat{X}(\sigma)$ and $\hat{Y}(\sigma)$ through a parameter σ .

In the following, examples of application of the optimization algorithm are presented by considering a uniform spacing $\Delta_{i+1}^{(\pm)} - \Delta_i^{(\pm)} = (\Delta_N^{(\pm)} - \Delta_0^{(\pm)})/N^{(\pm)}$ in the discretization, with $N^{(\pm)} = 120$, $\Delta_N^{(\pm)} = 2L$.

The following examples are also complemented by movies (available as electronic supplementary material) showing the theoretical behaviour of the structure optimized to display specific force-displacement curves.

5.1 The design of an elastic force-limiting device

In an ideal force-limiting device, the force P is expected to be initially linear with the displacement Δ , up to a threshold value at which the bifurcation occurs. Subsequently, the force is requested to remain

¹¹The profile can be designed for realizing a post-bifurcation response with incremental negative stiffness,

$$\frac{d\mathbf{p}^{(\pm)}(\Delta/L)}{d(\Delta/L)} < 0, \quad (82)$$

a concept under research for applications in vibration isolation and seismic engineering; see e.g. [2, 24, 32, 45].

constant (or slightly raise in its absolute value) at a further increase in the displacement magnitude, up to a point where the structure locks and the stroke of the device is attained. In practice however, a small increase in the force magnitude after buckling is desirable, to facilitate the return of the device to its initial configuration at unloading and to avoid snap motion due to negative stiffness. By excluding for the moment the final locking part, this behaviour can be described in mathematical terms as a symmetric bilinear force-displacement curve, namely, Eq. (75) with $p^{(\pm)}$ given as

$$p^{(\pm)}\left(\frac{\Delta}{L}; p_{cr}, r\right) = \pm p_{cr} + r \left(\frac{\Delta}{L} \mp p_{cr}\right), \quad (85)$$

where r is the bilinear stiffness ratio, relating the incremental constant stiffness in the post-buckling regime to that characterizing the structure before bifurcation (therefore enforced by Eq. (83) to $r < k_{\max} < 1$), and $p_{cr} = p_{cr}^{(+)} = -p_{cr}^{(-)}$.

The constraint's profile, which realizes a certain designed force-displacement behaviour (defined by p_{cr} and r), is not unique, rather, various shapes of the profile, realizing the target post-buckling behaviour $p^{(\pm)}$, can be found using the algorithm described in the previous section as a function of q .

A number of constraint's profile shapes are shown in Fig. 12 for $p_{cr} = \{0.01, 0.05, 0.3\}$ (from top to the bottom). The same force-displacement behaviour (reported in the insets) is obtained by changing q , assuming 2 pairs of values reported in each diagram. Profile shapes with different colours correspond to different values of bilinear stiffness ratio $r = \{-0.01, 0, 0.01\}$ (top), $r = \{-0.04, 0, 0.04\}$ (middle) and $r = \{-0.35, 0, 0.35\}$ (bottom).

Restricting attention to a null bilinear stiffness ratio, $r = 0$, the profile shapes are shown in Fig. 13 for $p_{cr} = 0.01$ (top left), $p_{cr} = 0.05$ (top right), and $p_{cr} = 0.3$ (bottom), for different values of the stiffness ratio q . The force-displacement diagrams are reported in the insets.

In both Figs. 12 and 13, some of the profile shapes and the corresponding load-displacement curves are ended with a marker (a cross or a circle). This marker shows the point where the optimization algorithm fails to converge because the target stiffness is too high (Issue 1, marked with a cross), or because a force reversal is found (Issue 3, marked with a circle). It should be noted that the blue curves in Fig. 12 show negative stiffness and therefore are unstable for imposed load p .

Also, small values of q provide smoother profiles than those obtained for large q . Moreover, small values of q lead to a large stroke, defined as the greatest displacement Δ reached with the device, see Fig. 13, showing that rod's extensibility facilitates the profile optimization. It is noted that small values of q can be obtained by using elements such as those described in Sect. 1.1. On the other hand, rods that are inextensible ($q \rightarrow \infty$) could be used to achieve the same effect, although inextensibility reduces the performance of the device.

For the practical realization of a force-limiter, a secondary increase in the stiffness has to be introduced in order to achieve a smooth transition to a maximum allowable displacement Δ_{\max} . This secondary increase in the stiffness can be achieved by modifying the final part of the profile shape. An example for $p_{cr} = 0.01$, $q = 10$, $r = 0$, and locking starting at $\Delta/L = \pm 0.73$ is shown in Fig. 1, along with the profile shape and the deformed configuration at $\Delta/L = \pm\{0.1, 0.2, 0.8\}$.

5.2 Profile shape for complex force-displacement curves

To show how far the present framework can be exploited to design constraint's profiles imposing highly complicated load-displacement curves, the present analysis is concluded by finding the profile shapes for a *sinusoidal* post-critical response (with constant average load),

$$p^{(\pm)}\left(\frac{\Delta}{L}; p_{cr}, a, b\right) = \pm p_{cr} + a \sin \left[2\pi b \left(\frac{\Delta}{L} \mp p_{cr}\right) \right] \quad (86)$$

and for a *triangular* post-critical response (with non-constant average load),

$$p^{(\pm)}\left(\frac{\Delta}{L}; p_{cr}, r_1, r_2, c\right) = \pm p_{cr} + r_1 \left(\frac{\Delta}{L} \mp p_{cr}\right) \mp r_2 \left| c \left(\frac{\Delta}{L} \mp p_{cr}\right) - \left[c \left(\frac{\Delta}{L} \mp p_{cr}\right) + \frac{1}{2} \right] \right|, \quad (87)$$

with the symbol $[\cdot]$ standing for the integer part of the relevant argument. Both the above design post-critical responses define a multistable element, where more than one stable displacement Δ exist at a given load p .

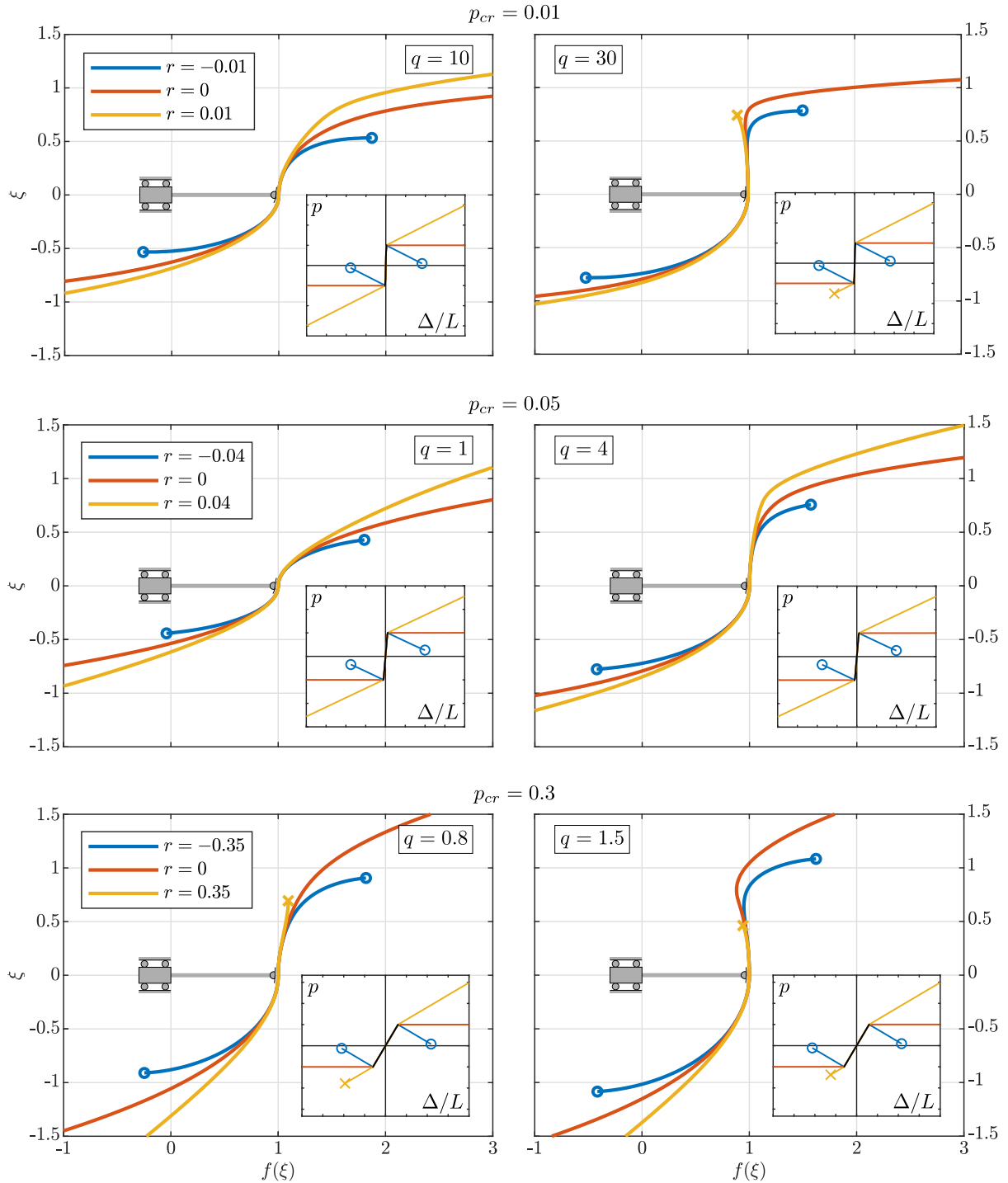


Figure 12: Profile's shapes realizing a symmetric bilinear force-displacement $p - \Delta$ curve (shown in the insets) with $p_{cr} = \{0.01, 0.05, 0.3\}$ (from top to the bottom) for three different values of the bilinear stiffness ratio $r = \{-0.01, 0, 0.01\}$ (top), $r = \{-0.04, 0, 0.04\}$ (middle) and $r = \{-0.35, 0, 0.35\}$ (bottom). Crosses and circles denote the points where the design $p - \Delta$ fails, putting out-of-service the device.

The profile shape for the sinusoidal response (86) with $a = 0.05$ and $b = 2$ is reported in Fig. 14 (upper row) while that for the triangular one (87) with $r_1 = 0.05$, $r_2 = 0.1$, and $c = 2$ in Fig. 14 (lower row). Two values of critical load are prescribed, $p_{cr} = 0.1$ (left) and $p_{cr} = 0.2$ (right), while the stiffness ratio assumes three values, $q = \{0.5, 1, 2\}$. Similarly to the bilinear post-critical response, also for these

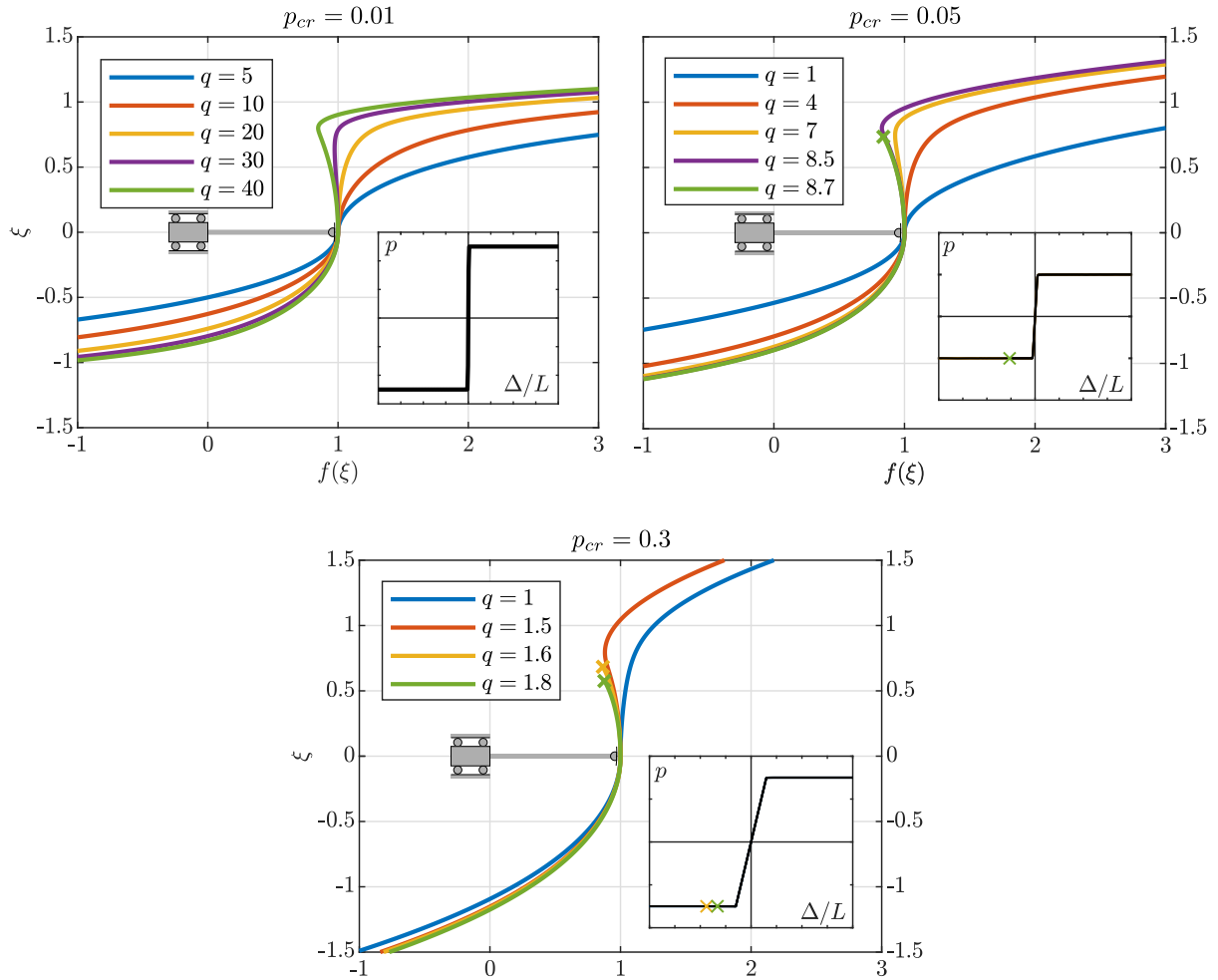


Figure 13: Profile’s shapes realizing a symmetric bilinear force-displacement $p - \Delta$ curve with null bilinear stiffness ratio (shown in the insets), $r = 0$, for $p_{cr} = 0.05$ (top left), $p_{cr} = 0.05$ (top right) and $p_{cr} = 0.3$ (bottom). Crosses denote the points where the design $p - \Delta$ fails, putting out-of-service the device. Note that small values of q extend the range of displacement for which the designed response is displayed.

other two cases, it is evident that the profile shape becomes smoother and can be defined for greater Δ and for small values of q .

6 Conclusions

The extensible elastica has been analytically solved with an end constrained to move along a curved frictionless profile (with or without a discontinuous curvature value in correspondence of the straight configuration). The solution for the full non-linear structural response has revealed the following features.

- The values of profile curvature at the origin $f''(0)$ and of axial/flexural stiffness ratio q have a significant effect on the existence, number, and value of the bifurcation loads, which may be compressive or tensile;
- When bifurcation in compression occurs, the system may display a single or a double restabilization of the straight configuration (occurring at large compression, depending on $f''(0)$ and q).

An optimization algorithm has been proposed for the design of the profile shape, to obtain a prescribed post-critical response. The optimization algorithm was positively tested to realize a large variety of load-displacement curves (bilinear, sinusoidal, triangular), useful for applications as force-limiter or other passive mechanisms.

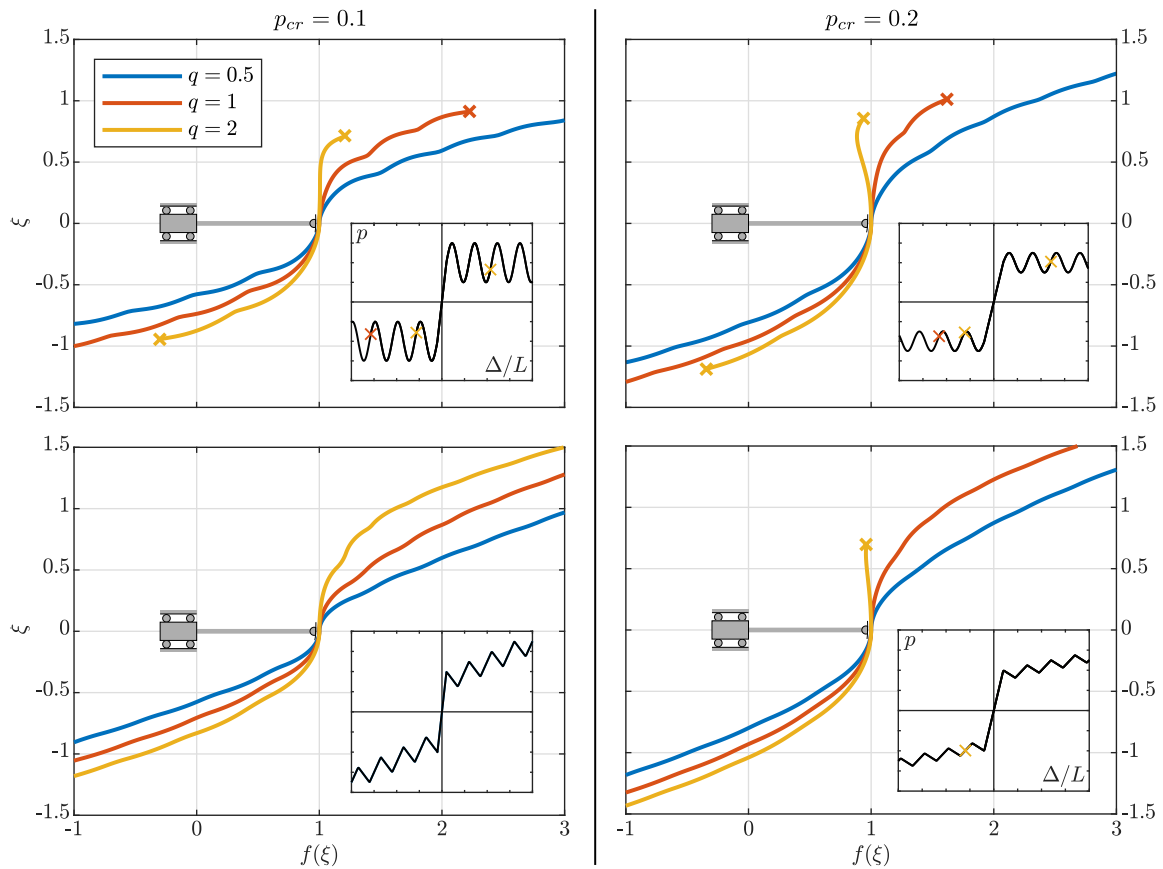


Figure 14: Constraint's profile shapes optimized for realizing (above) a sinusoidal force-displacement response, Eq. (86), with $a = 0.05$ and $b = 2$ and (bottom) a triangular response, Eq. (87), with $r_1 = 0.05$, $r_2 = 0.1$, and $c = 2$. Critical load is $p_{cr} = 0.1$ (left) and $p_{cr} = 0.2$ (right). Different shapes are reported for different values of the stiffness ratio q .

Acknowledgements

PK and FDC gratefully acknowledge the financial support from the European Union's Horizon 2020 research and innovation programme under the Marie Skłodowska-Curie grant agreement 'INSPIRE - Innovative ground interface concepts for structure protection' PITN-GA-2019-813424-INSPIRE. DB gratefully acknowledges financial support from ERC-ADG-2021-101052956-BEYOND. Support from the Italian Ministry of Education, University and Research (MIUR) in the frame of the 'Departments of Excellence' grant L. 232/2016 is acknowledged. This work has been developed under the auspices of INDAM-GNFM.

PK would like to thank Samuele Infanti (FIP MEC, Padova, Italy) for the useful discussions on technological aspects of the device design and realization.

DB and FDC acknowledge the in-depth discussions and fruitful collaboration through these years with Natasha and Sasha. They look forward to many more years of enjoying together stimulating scientific interaction and friendship.

References

- [1] P.M. Alabuzhev and E.I. Rivin. *Vibration Protection And Measuring Systems With Quasi-Zero Stiffness*. Applications of Vibration Series. Taylor & Francis, 1989. ISBN: 9780891168119. URL: <https://books.google.it/books?id=bBwqumyTAgUC>.

- [2] Ioannis A. Antoniadis et al. “KDamping: A stiffness based vibration absorption concept”. In: *Journal of Vibration and Control* 24 (2018), pp. 588–606.
- [3] C. Armanini et al. “Configurational forces and nonlinear structural dynamics”. In: *Journal of the Mechanics and Physics of Solids* 130 (2019), pp. 82–100. ISSN: 0022-5096. DOI: <https://doi.org/10.1016/j.jmps.2019.05.009>. URL: <https://www.sciencedirect.com/science/article/pii/S0022509619301346>.
- [4] Milan Batista. “A closed-form solution for Reissner planar finite-strain beam using Jacobi elliptic functions”. In: *International Journal of Solids and Structures* 87 (2016), pp. 153–166.
- [5] Farid Bendjellal et al. “The combination of a new air bag technology with a belt load limiter”. In: *Proc. of the 16th Int. Technical Conf. on the Enhanced Safety of Vehicles*. 1998.
- [6] D Bigoni et al. “Effects of the constraint’s curvature on structural instability: tensile buckling and multiple bifurcations”. In: *Proceedings of the Royal Society A: Mathematical, Physical and Engineering Sciences* 468.2144 (2012), pp. 2191–2209.
- [7] D Bigoni et al. “Instability of a penetrating blade”. In: *Journal of the Mechanics and Physics of Solids* 64 (2014), pp. 411–425.
- [8] D. Bigoni et al. “New phenomena in nonlinear elastic structures: from tensile buckling to configurational forces”. In: *Extremely Deformable Structures*. Ed. by Davide Bigoni. Vienna: Springer Vienna, 2015, pp. 55–135. ISBN: 978-3-7091-1877-1. DOI: 10.1007/978-3-7091-1877-1_2. URL: https://doi.org/10.1007/978-3-7091-1877-1_2.
- [9] F Bosi et al. “Self-encapsulation, or the ‘dripping’ of an elastic rod”. In: *Proceedings of the Royal Society A: Mathematical, Physical and Engineering Sciences* 471.2179 (2015), p. 20150195.
- [10] F. Bosi et al. “Asymptotic self-restabilization of a continuous elastic structure”. In: *Phys. Rev. E* 94 (6 Dec. 2016), p. 063005. DOI: 10.1103/PhysRevE.94.063005. URL: <https://link.aps.org/doi/10.1103/PhysRevE.94.063005>.
- [11] F. Bosi et al. “Development of configurational forces during the injection of an elastic rod”. In: *Extreme Mechanics Letters* 4 (2015), pp. 83–88. ISSN: 2352-4316. DOI: <https://doi.org/10.1016/j.eml.2015.04.007>. URL: <https://www.sciencedirect.com/science/article/pii/S2352431615000656>.
- [12] Matthew L Brumbelow, Bryan C Baker, and Joseph M Nolan. “Effects of seat belt load limiters on driver fatalities in frontal crashes of passenger cars”. In: *International Technical Conference on the Enhanced Safety of Vehicles, Paper. 07-0067*. 2007.
- [13] A Carrella, MJ Brennan, and TP Waters. “Static analysis of a passive vibration isolator with quasi-zero-stiffness characteristic”. In: *Journal of sound and vibration* 301.3-5 (2007), pp. 678–689.
- [14] Louis D’Aulerio et al. “Forensic Performance Analysis of Load-Limiting Devices in Automotive Seat Belt Retractors”. In: *Journal of forensic sciences* 64.3 (2019), pp. 754–764.
- [15] Riccardo DeSalvo. “Passive, nonlinear, mechanical structures for seismic attenuation”. In: (2007).
- [16] JA Haringx. “Instability of springs”. In: *Philips Tech. Rev.* 11 (1950), pp. 245–251.

- [17] JA Haringx. “On highly compressible helical springs and rubber rods, and their application for vibration-free mountings”. In: *Philips Res. Rep.* 3 (1948), pp. 401–449.
- [18] Alexander Humer. “Elliptic integral solution of the extensible elastica with a variable length under a concentrated force”. In: *Acta mechanica* 222.3 (2011), pp. 209–223.
- [19] Alexander Humer. “Exact solutions for the buckling and postbuckling of shear-deformable beams”. In: *Acta Mechanica* 224.7 (2013), pp. 1493–1525.
- [20] RA Ibrahim. “Recent advances in nonlinear passive vibration isolators”. In: *Journal of sound and vibration* 314.3-5 (2008), pp. 371–452.
- [21] Lishuai Jin et al. “Guided transition waves in multistable mechanical metamaterials”. In: *Proceedings of the National Academy of Sciences* 117.5 (2020), pp. 2319–2325.
- [22] Konstantinos A. Kapasakalis, Ioannis A. Antoniadis, and Evangelos J. Sapountzakis. “KDamper Concept for Base Isolation and Damping of High-Rise Building Structures”. In: *Proceedings of the 14th International Conference on Vibration Problems*. Ed. by Evangelos J. Sapountzakis et al. Singapore: Springer Singapore, 2021, pp. 265–289. ISBN: 978-981-15-8049-9.
- [23] V Kobelev. *Durability of Springs*. Springer International Publishing, 2021. ISBN: 9783030592530. URL: <https://books.google.it/books?id=0BwgEAAAQBAJ>.
- [24] Xingtian Liu, Xiuchang Huang, and Hongxing Hua. “On the characteristics of a quasi-zero stiffness isolator using Euler buckled beam as negative stiffness corrector”. In: *Journal of Sound and Vibration* 332.14 (2013), pp. 3359–3376.
- [25] Jiayao Ma, Jichao Song, and Yan Chen. “An origami-inspired structure with graded stiffness”. In: *International Journal of Mechanical Sciences* 136 (2018), pp. 134–142.
- [26] Anders Magnusson, Matti Ristinmaa, and Christer Ljung. “Behaviour of the extensible elastica solution”. In: *International Journal of Solids and Structures* 38.46-47 (2001), pp. 8441–8457.
- [27] H Mori et al. “The effect of beam inclination on the performance of a passive vibration isolator using buckled beams”. In: *Journal of Physics: Conference Series*. Vol. 744. 1. IOP Publishing. 2016, p. 012229.
- [28] Alf Pflüger. *Stabilitätsprobleme der Elastostatik*. Springer-Verlag, 2013.
- [29] Eric Reissner. “On one-dimensional finite-strain beam theory: the plane problem”. In: *Zeitschrift für angewandte Mathematik und Physik ZAMP* 23.5 (1972), pp. 795–804.
- [30] Eugene I Rivin. *Passive vibration isolation*. Amer Society of Mechanical, 2003.
- [31] W Robertson et al. “Zero-stiffness magnetic springs for active vibration isolation”. In: (2006).
- [32] EJ Sapountzakis et al. “KDamper concept in seismic isolation of bridges with flexible piers”. In: *Engineering Structures* 153 (2017), pp. 525–539.
- [33] Sicong Shan et al. “Multistable architected materials for trapping elastic strain energy”. In: *Advanced Materials* 27.29 (2015), pp. 4296–4301.
- [34] James Johnston Stoker. *Nonlinear elasticity*. Gordon and Breach, 1968.
- [35] Ran Tao et al. “4D printed multi-stable metamaterials with mechanically tunable performance”. In: *Composite Structures* 252 (2020), p. 112663.

- [36] Ran Tao et al. “4D printed origami metamaterials with tunable compression twist behavior and stress-strain curves”. In: *Composites Part B: Engineering* 201 (2020), p. 108344. ISSN: 1359-8368. DOI: <https://doi.org/10.1016/j.compositesb.2020.108344>. URL: <https://www.sciencedirect.com/science/article/pii/S135983682033393X>.
- [37] LN Virgin, ST Santillan, and RH Plaut. “Vibration isolation using extreme geometric nonlinearity”. In: *Journal of Sound and Vibration* 315.3 (2008), pp. 721–731.
- [38] Mondrus Vladimir and Smirnov Vladimir. “Optical tables vibration isolation during precision measurements”. In: *Procedia Engineering* 111 (2015), pp. 561–568.
- [39] AM Wahl. *Mechanical Springs*. McGraw-Hill, 1963. URL: <https://books.google.it/books?id=ATpSAAAAMAAJ>.
- [40] John Winterflood, David Gerald Blair, and Bram Slagmolen. “High performance vibration isolation using springs in Euler column buckling mode”. In: *Physics Letters A* 300.2-3 (2002), pp. 122–130.
- [41] Hang Yang and Li Ma. “Multi-stable mechanical metamaterials by elastic buckling instability”. In: *Journal of materials science* 54.4 (2019), pp. 3509–3526.
- [42] Xianglong Yu et al. “Mechanical metamaterials associated with stiffness, rigidity and compressibility: A brief review”. In: *Progress in Materials Science* 94 (2018), pp. 114–173.
- [43] Daniele Zaccaria et al. “Structures buckling under tensile dead load”. In: *Proceedings of the Royal Society A: Mathematical, Physical and Engineering Sciences* 467.2130 (2011), pp. 1686–1700.
- [44] Quan Zhang, Dengke Guo, and Gengkai Hu. “Tailored Mechanical Metamaterials with Programmable Quasi-Zero-Stiffness Features for Full-Band Vibration Isolation”. In: *Advanced Functional Materials* 31.33 (2021), p. 2101428.
- [45] Yisheng Zheng et al. “Design and experiment of a high-static–low-dynamic stiffness isolator using a negative stiffness magnetic spring”. In: *Journal of Sound and Vibration* 360 (2016), pp. 31–52.
- [46] N Zhou and K Liu. “A tunable high-static–low-dynamic stiffness vibration isolator”. In: *Journal of Sound and Vibration* 329.9 (2010), pp. 1254–1273.

A Examples of one-dimensional structures displaying small values of stiffness ratio q

To further substantiate the examples introduced in Sect. 1.1, a stiffness ratio evaluation is provided. The evaluation is based on the shear stiffness K_s , axial stiffness K_a (corresponding to K in the main text), and bending stiffness B of the Reissner beam equivalent to a helical spring [23]

$$K_s^{\text{spring}} = \frac{8EI_r L}{\pi n_a D^3}, \quad K_a^{\text{spring}} = \frac{4GI_T L}{\pi n_a D^3}, \quad B^{\text{spring}} = \frac{2EIL}{\pi n_a D \left(1 + \frac{EI}{GI_T}\right)}, \quad (\text{A.1})$$

where E is the Young’s modulus, G the shear modulus, I is the moment of inertia of the wire cross-section with respect to the radius of the spring coil passing through the centre of the cross-section, I_r is the moment of inertia of the wire cross-section with respect to the axis perpendicular to the radius passing through the centre of the cross-section, I_T is the torsion constant, L is the length of the spring, D is the coil diameter, and n_a is the number of (active) coils.

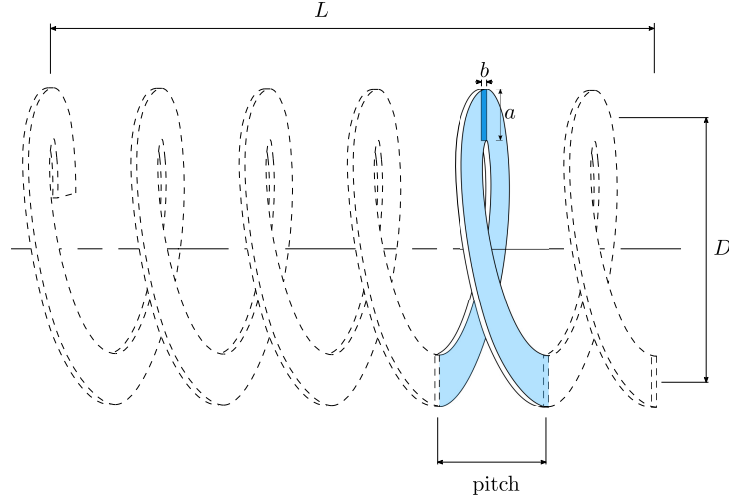


Figure A.1: A rectangular wire helical spring realizing an equivalent one-dimensional rod with very small ratios between axial and bending/shear stiffnesses.

The dimensionless axial stiffness parameter q_a (corresponding to q in our manuscript) and shear stiffness parameter q_s are introduced as

$$q_a = \frac{K_a L^2}{\pi^2 B}, \quad q_s = \frac{K_s L^2}{\pi^2 B}, \quad (\text{A.2})$$

which reduce for a helical spring to

$$q_a^{\text{spring}} = \frac{2}{\pi^2} \left(1 + \frac{GI_T}{EI} \right) \left(\frac{L}{D} \right)^2, \quad q_s^{\text{spring}} = \frac{2EI_T}{GI_T} q_a^{\text{spring}}. \quad (\text{A.3})$$

Interestingly, the ratio between the two stiffness ratios is given by

$$\frac{q_a^{\text{spring}}}{q_s^{\text{spring}}} = \frac{GI_T}{2EI_r}. \quad (\text{A.4})$$

We are now in a position to quantify the value of q for the two cases below.

A.1 Rectangular wire helical springs

For a rectangular wire of edges a and b , as illustrated in Fig. A.1, the moments of inertia are given by

$$I = \frac{ab^3}{12}, \quad I_r = \frac{a^3b}{12}, \quad (\text{A.5})$$

and, in the considered case $a > b$ the torsion constant by

$$I_T \approx \left[1 - 0.63 \frac{b}{a} + 0.052 \left(\frac{b}{a} \right)^5 \right] \frac{ab^3}{3}. \quad (\text{A.6})$$

Considering a steel spring ($E = 2.6 G$, with G being the shear modulus) and characterized by $L = 5D$ (similarly to examples reported in [16, 17, 39]), the stiffness ratios q_a^{spring} and q_s^{spring} are shown in Fig. A.2 as increasing functions of the aspect ratio a/b of the rectangular cross section.

Finally, considering for example an aspect ratio $a/b = 8$ and setting the height b of the wire such that the ratio between b and the pitch of the coil is $1/20$, the corresponding spring (shown in Fig. A.1) can be compressed up to 95% of its undeformed length and is characterized by the two following stiffness ratios

$$q_a^{\text{spring}} = 1.225 \cdot 10, \quad q_s^{\text{spring}} = 1.103 \cdot 10^3, \quad (\text{A.7})$$

providing values for an equivalent rod with negligible shear effects and that could be modelled as the extensible elastica.

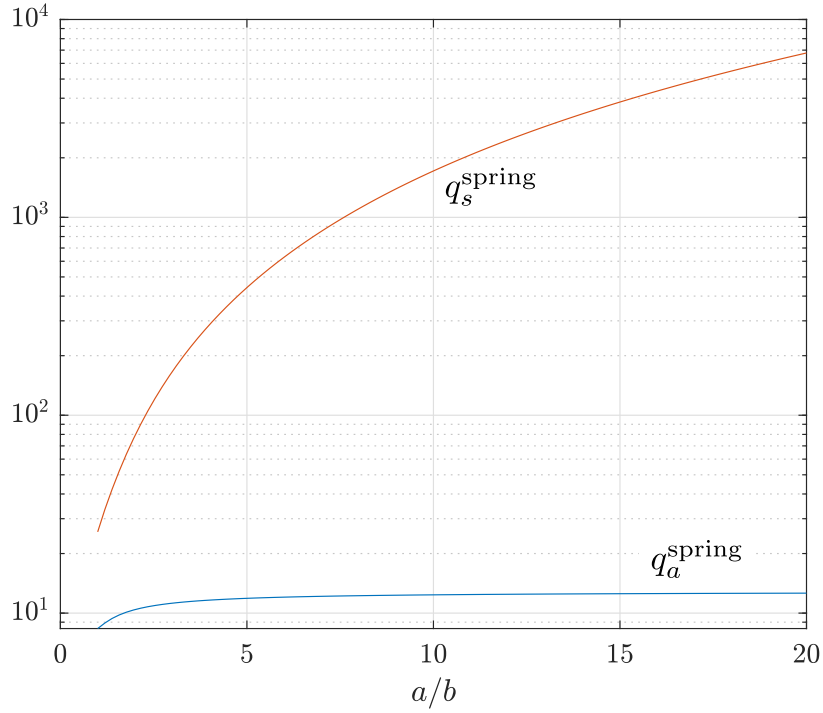


Figure A.2: Semi-logarithmic plot of the stiffness ratios q_a^{spring} and q_s^{spring} for a rectangular wire helical spring, as functions of the aspect ratio a/b of the rectangular wire cross-section with $L/D = 5$ (reported in Fig. A.1 for $a/b = 8$).

A.2 Composite rod-spring element

A helical spring is considered to contain a coaxial elastic rod, as shown in Fig. A.3. While one end of the spring is fixed to the corresponding end of the rod, the remaining part of the spring can slide without friction along the rod.¹² Assuming that the spring and the rod react in parallel, the shear and bending stiffnesses of the equivalent one-dimensional element, working as an axially-deformable elastica, are simply the sum of that of the spring and of the rod, namely

$$K_s = K_s^{\text{rod}} + K_s^{\text{spring}}, \quad B = B^{\text{rod}} + B^{\text{spring}}, \quad (\text{A.8})$$

¹²Although frictionless, the moving boundary problem realized through the relative motion of the spring with respect to the rod may realize configurational forces, whenever a non-null rod's curvature is displayed. Nevertheless, due to their higher-order character, such configurational forces do not affect the buckling analysis and therefore can be neglected [7]. This implies that the double restabilization feature is not compromised, so that only the post-buckling response changes.

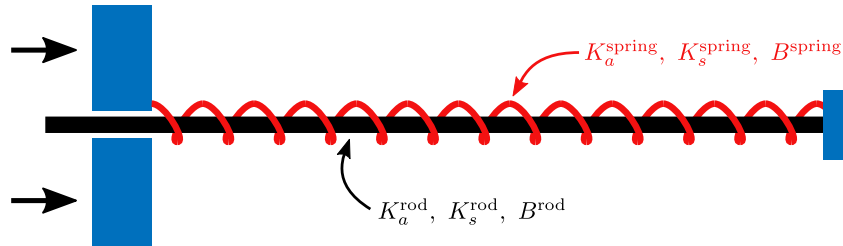


Figure A.3: A one-dimensional element working as an axially-deformable elastica, characterized by high shear stiffness ratio q_s but low axial stiffness ratio q_a , obtained as an elastic rod inserted within a helical spring. The spring can slide along the rod so that the latter does not contribute to the axial stiffness of the structure.

while, considering that loads are applied on the spring, the equivalent axial stiffness coincides with that of the spring because of its frictionless sliding along the rod,

$$K_a = K_a^{\text{spring}}. \quad (\text{A.9})$$

It follows that the axial stiffness can be tuned independently of the bending and shear stiffnesses, to attain (almost) any pair of desired stiffness ratios q_a and q_s .

As an example for a round wire spring, the axial, shear and bending stiffnesses are given by

$$K_a^{\text{spring}} = \frac{Gd^4L}{8n_aD^3}, \quad K_s^{\text{spring}} = \frac{Ed^4L}{8n_aD^3}, \quad B^{\text{spring}} = \frac{Ed^4L}{32\left(1 + \frac{E}{2G}\right)n_aD}, \quad (\text{A.10})$$

and for a circular rod of diameter D^{rod} as

$$K_s^{\text{rod}} = \frac{8\pi G (D^{\text{rod}})^2}{37}, \quad B^{\text{rod}} = \frac{\pi E (D^{\text{rod}})^4}{64}, \quad (\text{A.11})$$

where for simplicity the rod and the spring have been considered as made up of the same material (differently, the selection of a material for the rod stiffer than that constituting the spring, $E^{\text{rod}} > E^{\text{spring}}$ further facilitates satisfaction of the inequality $q_a \ll q_s$ with $q_a \approx 10$). The stiffness ratios of the equivalent one-dimensional element become

$$q_a = \frac{4G}{\pi^2 n_a E \beta} \left(\frac{d}{D}\right)^4 \left(\frac{L}{D}\right)^3, \quad (\text{A.12})$$

$$q_s = \frac{1}{\pi^2 \beta} \left(\frac{L}{D}\right)^2 \left[\frac{4}{n_a} \left(\frac{d}{D}\right)^4 \left(\frac{L}{D}\right) + \frac{256\pi G}{37E} \left(\frac{D^{\text{rod}}}{D}\right)^2 \right],$$

where

$$\beta = \frac{1}{\left(1 + \frac{E}{2G}\right)n_a} \left(\frac{d}{D}\right)^4 \left(\frac{L}{D}\right) + \frac{\pi}{2} \left(\frac{D^{\text{rod}}}{D}\right)^4. \quad (\text{A.13})$$

The stiffness ratios described by Eq. (A.12) are shown in Fig. A.4 as monotonic increasing functions of the ratio L/D , by assuming $d/D = 0.1$, $D^{\text{rod}}/D = 0.8$ and the pitch of the coil has been selected in order to have 95% maximum compression with respect to the undeformed length. Finally, assuming for example $L/D = 50$, the stiffness ratios are

$$q_a = 1.211 \cdot 10^{-1}, \quad q_s = 2.107 \cdot 10^3, \quad (\text{A.14})$$

corresponding to values of an equivalent rod with negligible shear effects and that could be properly modelled through the extensible elastica considered in the present paper.

B Asymptotic behaviour of bifurcation load for vanishing profile curvature at the origin

Asymptotic expressions for the bifurcation load in the limit of vanishing profile curvature at the origin can be obtained by solving the first-order expansion in $f''(0) \rightarrow 0^\pm$ of Eq. (26). It follows that the critical load under tension has the following singular asymptote¹³

$$\lim_{f''(0) \rightarrow 0^-} p_{cr}^{(+)} = -\frac{1}{f''(0)} - 1 - \frac{\text{sgn}(f''(0))}{\pi\sqrt{q}}. \quad (\text{B.1})$$

Concerning the bifurcation loads under compression, $p \in (-1, 0)$, the asymptotic behaviour determines the presence of two critical loads (corresponding to destabilization and restabilization of the trivial

¹³The asymptotic expression (B.1) also holds for p within the (meaningless) range $(-\infty, -1] \cup [0, \infty)$, as it can be appreciated from Fig. B.1.

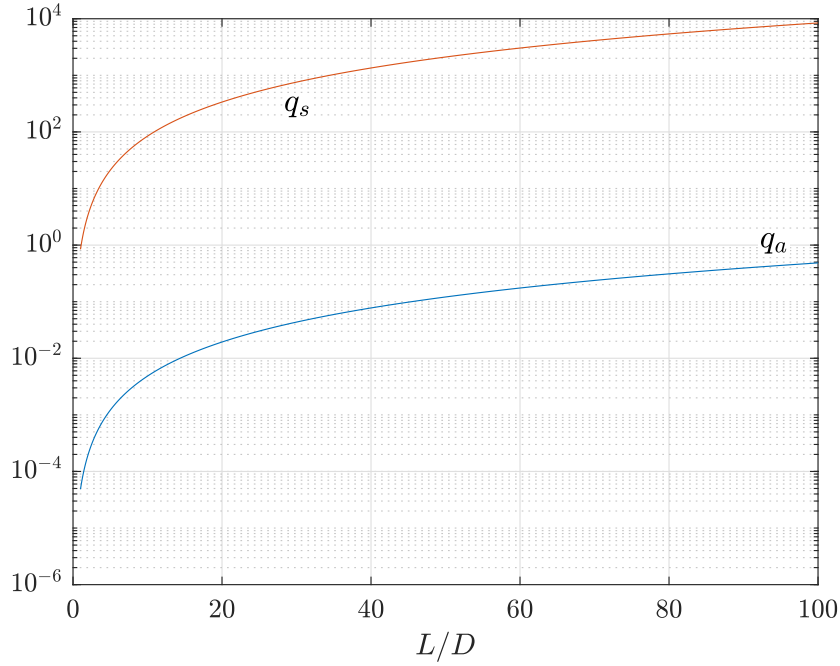


Figure A.4: Semi-logarithmic plot of the stiffness ratios q_a and q_s for a composite rod-spring element (Fig. A.3) as functions of L/D .

configuration) for a number N of critical modes depending on q . The asymptotic expression for the destabilization $p_{de}^{(-)[n]}$ and restabilization $p_{re}^{(-)[n]}$ loads, pertaining to the n -th mode, results to be a finite value independent of the sign of the profile curvature

$$\lim_{f''(0) \rightarrow 0^+} \{p_{de}^{(-)[n]}, p_{re}^{(-)[n]}\} = \lim_{f''(0) \rightarrow 0^-} \{p_{de}^{(-)[n]}, p_{re}^{(-)[n]}\} = \frac{1}{2} \left(-1 \pm \frac{\sqrt{-1 - 4n - 4n^2 + q}}{\sqrt{q}} \right), \quad (\text{B.2})$$

where the number N of existing critical modes is given by

$$N = \max \left\{ \left\lfloor \frac{\sqrt{q} - 1}{2} \right\rfloor, 0 \right\}, \quad (\text{B.3})$$

with the symbol $\lfloor \cdot \rfloor$ standing for the integer part of the relevant argument.

It is interesting to note that in the limit of $f''(0) \rightarrow 0^\pm$ the structure reduces to an extensible rod connected to a sliding clamp on its left end and with the right end constrained only in the horizontal direction. In this case, the tensile bifurcation load approaches infinity ($p_{cr}^{(+)} \rightarrow \infty$), so that tensile buckling is excluded.

Finally, the compressive bifurcation loads in the inextensible limit ($q \rightarrow \infty$) match those pertaining to a cantilever Euler beam (with clamped-free boundary conditions),

$$\lim_{q \rightarrow \infty} \{P_{de}^{(-)[n]}\} = -\frac{(2n+1)^2 \pi^2 B}{4L^2}, \quad (\text{B.4})$$

while restabilization does not occur because the corresponding load assumes a negative infinite value

$$\lim_{q \rightarrow \infty} \{P_{re}^{(-)[n]}\} = -\infty. \quad (\text{B.5})$$

As an example, the bifurcation conditions for the dimensionless load pq with varying the dimensionless radius of profile curvature $1/f''(0)$ are reported in Fig. B.1 for $q = 10$ (left) and for $q = 400$ (right). It can be appreciated that the asymptotic behaviour (drawn as dashed lines) for $1/f''(0) \rightarrow \pm\infty$ is symmetric in the range $p \in [-1, 0]$, as predicted by Eq. (B.2), and that only one asymptote exists for $1/f''(0) \rightarrow -\infty$ for positive p , as predicted by Eq. (B.1).

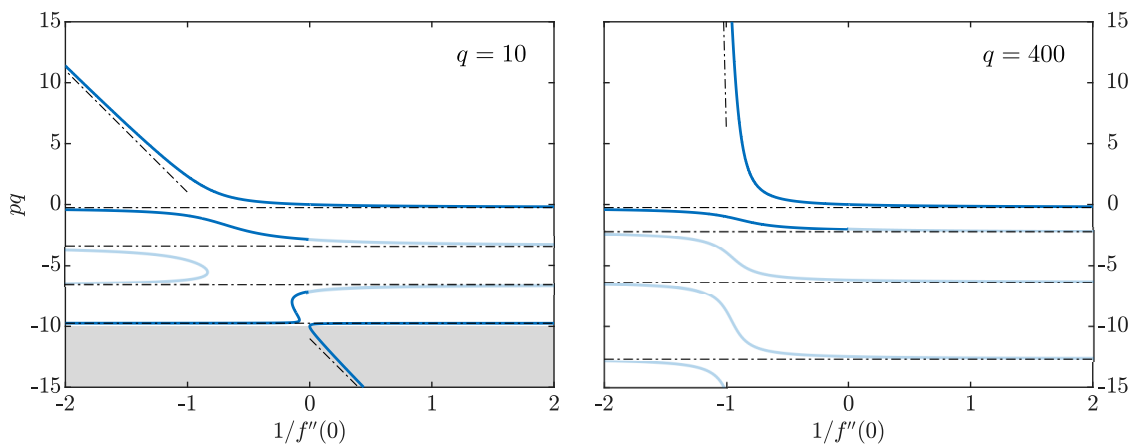


Figure B.1: Bifurcation dimensionless load $pq = PL^2/(\pi^2 B)$ as a function of the dimensionless radius of profile curvature at the origin, $1/f''(0)$, for fixed values of q , ($q = 10$ on the left and $q = 400$ on the right). The asymptotic behaviour, Eqs. (B.1) and (B.2), is represented by dashed lines.